



Thermodynamic analysis of HP-UHP fluid inclusions: The solute load and chemistry of metamorphic fluids

A. Maffeis^{a,*}, S. Ferrando^{a,*}, J.A.D. Connolly^b, C. Groppo^{a,c}, M.L. Frezzotti^d,
D. Castelli^a

^a University of Torino, Department of Earth Sciences, Via Valperga Caluso, 35, I-10125 Torino, Italy

^b ETH Zurich, Department of Earth Sciences, Institute for Geochemistry and Petrology, Clausiusstrasse 25, CH 8092 Zurich, Switzerland

^c C.N.R. – I.G.G., Section of Torino, Via Valperga Caluso 35, I-10125 Torino, Italy

^d University of Milano-Bicocca, Department of Environment and Earth Sciences, Piazza della Scienza 4, 20126 Milano, Italy

Received 19 February 2021; accepted in revised form 31 August 2021; available online xxx

Abstract

Subduction fluids play a crucial role in regulating long-term chemical cycles. Their characterisation is essential to understand the processes responsible for metasomatism, oxidation and melting of the mantle wedge. Both direct (fluid inclusion studies) and indirect (thermodynamic modelling) approaches to study subduction fluids have reliability issues due to the complexity of the investigated processes. Post-entrapment processes (e.g., solvent loss by diffusion or decrepitation and/or chemical reactions between host mineral and trapped fluid) are likely to modify the chemical fingerprint of ultra-high pressure (UHP) fluid inclusions, while thermodynamic modelling of solute-bearing fluids at UHP conditions is still at the beginning of its application. In this work, we apply and compare data obtained by both approaches for fluid inclusions trapped within UHP clinopyroxene from a chemically simple Ol-Cpx-Dol-Cal marble (Brossasco-Isasca Unit, Dora-Maira Massif, Western Italian Alps). Classical molecular-fluid thermodynamics is adequate to qualitatively describe the post-entrapment reactions between fluid inclusions and host clinopyroxene. However, an electrolytic fluid model is necessary to describe the chemical composition of the solute-bearing aqueous fluids at the peak metamorphic condition (H₂O: 96.30 mol%/88.49 wt%; solutes: 3.61 mol%/11.34 wt%/2.08 mol/kg; other volatiles: 0.09 mol%/0.17 wt%) generated by progressive rock dissolution. Comparison of the model fluid composition with that inferred from the analysis of fluid inclusions clarifies the types and the extent of post-trapping chemical modification of the UHP fluid inclusions. Our data reveal that the fluid-host reactions carry up to 42 mol% of host clinopyroxene component in the fluid inclusion bulk composition, whereas the fluid inclusion decrepitation and the water diffusion in the host clinopyroxene (through dislocations and/or micro-fractures) cause an H₂O loss ranging from 18 mol% to 99 mol%. Applying these approaches, we demonstrate that the most relevant post-entrapment process is H₂O loss. We also demonstrate that some fluid inclusions did not experience post-entrapment fluid-host modification and, thus, preserve the original fluid geochemistry.

© 2021 Elsevier Ltd. All rights reserved.

Keywords: Fluid inclusions; Electrolytic-fluid thermodynamics; C-bearing subduction fluid; Dora-Maira marble; Ultra-High Pressure

1. INTRODUCTION

The physicochemical characterisation of the fluids released during deep subduction of both oceanic and continental crust is essential to understand the processes active

* Corresponding authors.

E-mail addresses: andrea.maffeis@unito.it (A. Maffeis), simona.ferrando@unito.it (S. Ferrando).

<https://doi.org/10.1016/j.gca.2021.08.044>

0016-7037/© 2021 Elsevier Ltd. All rights reserved.

at convergent margins and responsible for long-term chemical cycles (i.e., H, C, S and N Cycles: Kelemen and Manning, 2015; Karlsen et al., 2019; Plank and Manning, 2019; Mysen, 2019; Manning and Frezzotti, 2020; Li et al., 2020a,b). Subduction-derived fluids are responsible for metasomatism, oxidation and melting of the overlying mantle wedge (e.g., Manning, 2004; Bebout, 2013; Tumiati and Malaspina, 2019) and, ultimately, for magmatism at convergent margins (e.g., Peccerillo and Frezzotti, 2015). Natural, theoretical, and experimental investigations indicate that metamorphic fluids are often composed predominantly of C-O-H-N-S molecular volatiles. Subordinate to high amounts of organic acids and hydrocarbons (Brovarone et al., 2017; Huang et al., 2017; Li, 2017; Frezzotti 2019) and non-volatile elements (e.g., Si, Al, Ca, Mg, Fe, K, Na, Cl), dissolved as molecular and ionic species bounded to S-Cl-Si-C ligands (i.e., SO_4 , HCO_3^- , CO_3^{2-} ; HSiO_3 , Cl; Philippot and Selverstone, 1991; Philippot et al. 1995; Frezzotti et al., 2011; Sanchez-Valle, 2013; Frezzotti and Ferrando, 2015) are also observed in natural and experimental fluids and predicted by recent thermodynamic models (Huang and Sverjensky, 2019; Guild and Shock, 2020).

Direct information on deep fluids can only be derived from fluid inclusions (FIs) trapped during the growth of high pressure and ultra-high pressure (HP-UHP) minerals (Philippot et al. 1995; Stöckhert et al., 2001; Zhang et al., 2008; Frezzotti et al., 2011; Frezzotti and Ferrando, 2015; Vitale Brovarone et al., 2017; Kawamoto et al., 2018; Frezzotti, 2019; Bodnar and Frezzotti, 2020). Ideally, FIs trapped during deep subduction should reach ambient *P-T* conditions following an isochoric decompression without any post-trapping modifications (Roedder, 1984; Touret, 2001; Supplementary Fig. 1). Actually, each FI usually experiences an early near-isothermal decompression followed by an isochoric decompression (Touret, 2001; Supplementary Fig. 1). Concerning the ideal isochoric decompression, this complex path promotes modifications on density (whose study is out of the scope of this work) and on the chemistry of the HP-UHP FI. Chemical modification can be cryptic (i.e., solvent loss by diffusion; not visible under the microscope) or non-cryptic (i.e., fluid-host reaction and solvent loss along micro fractures; visible under the microscope). Being H_2O the dominant solvent component at sub-solidus conditions, diffusion of H^+ , OH^- , H_2 , or H_2O out of the FI through the host-mineral lattice or along dislocations is a common process (e.g., Bakker and Jansen, 1990,1991; Hall and Sterner, 1993; Mavrogenes and Bodnar, 1994; Viti and Frezzotti, 2000; Bakker, 2009; Frezzotti et al. 2012a). The subsequent chemical modification of the trapped fluid implies its relative enrichment in the residual elements without changing their relative proportions (e.g., the dehydration trend of Frezzotti et al., 2012a). Non-cryptic modifications are caused by decrepitation or reaction between the trapped HP-UHP fluid and the host mineral. Decrepitation can occur during exhumation if the FI internal pressure becomes higher than the external confining pressure. This process will cause a partial loss of fluid from the FI. In minerals able to chemically interact with the trapped fluid

(e.g., clinopyroxene, garnet, olivine, orthopyroxene; Andersen et al., 1984; Heinrich and Gottschalk, 1995; Frezzotti et al., 2012a; Frezzotti and Ferrando, 2015; Carvalho et al., 2020), “step-daughter minerals” (Svensen et al., 1999) could be produced by fluid-host reactions, and they must be distinguished from proper “daughter minerals” (i.e., precipitated from the trapped fluid).

An indirect approach to the study of metamorphic fluids is thermodynamic modelling. At HP-UHP conditions, the transfer of rock-forming elements from the rock matrix to the fluid mainly occurs via mineral dissolution (e.g., Ferrando et al., 2017, 2019), and this process cannot be modelled with classical molecular fluid models. Currently, the Helgeson-Kirkham-Flowers EOS for aqueous species as adapted in the Deep Earth Water model (DEW-HKF; Helgeson and Kirkham, 1974a, 1974b, 1976, 1981; Sverjensky et al., 2014; Connolly and Galvez, 2018) is the only fluid model capable of accounting for non-volatile solutes in fluids released during deep subduction. In this model, the activities of non-volatile elements, dissolved as molecular and ionic species, are computed relative to the solute standard state. In contrast, the properties of molecular volatiles (i.e., CO_2 , CH_4 , H_2S , etc.) may be computed relative to either the solvent or solute standard state (Connolly and Galvez, 2018).

Carbonate lithologies are rarely considered to release fluids at HP-UHP conditions because of the lack of relevant decarbonation reactions during subduction. Nevertheless, the carbonate dissolution by aqueous fluids is an alternative and less explored mechanism for carbon mobilisation in subduction fluids (e.g., Frezzotti et al., 2011; Ague and Nicolescu, 2014; Kelemen and Manning, 2015; Ferrando et al., 2017; Menzel et al., 2020; Farsang et al., 2021). The role of both carbonatic and carbonated sediments must be considered because, although they roughly represent ~10% of the thickness of the average subducted oceanic lithosphere at the trench, they constitute up to ~68% of the annual influx of C in subduction zones (Kelemen and Manning, 2015; Clift, 2017; Plank and Manning, 2019; Bekaert et al., 2020).

In the present work, we studied the FIs occurring in UHP clinopyroxene (diopside) porphyroblasts from a chemically simple impure marble (calcite, dolomite, clinopyroxene, olivine) from Costa Monforte, in the UHP Brossasco-Isasca Unit of the southern Dora-Maira Massif (Western Italian Alps). This marble experienced multiple carbonate dissolution-precipitation events during active subduction (Ferrando et al., 2017). Because the host clinopyroxene is a mineral that facilitates post-entrapment modifications (i.e., fluid-host reactions and H_2O loss by diffusion and decrepitation), a thermodynamic evaluation (through molecular-fluid thermodynamics) of possible post-entrapment reactions has been performed. Moreover, electrolytic-fluid thermodynamics has been applied to model the composition of the UHP fluid in equilibrium with the mineral assemblages at peak metamorphic conditions. Comparing the fluid compositions reconstructed from FIs and those modelled through electrolytic-fluid thermodynamics allowed: (i) to recognise the extent of the post-entrapment modifications experienced by the studied FI,

and (ii) to identify the types of the occurred post-entrapment chemical re-equilibrations. These results highlight the reliability of both the direct and indirect approaches to the chemical characterisation of the fluids released during deep subduction of both oceanic and continental crust.

2. METHODS

2.1. Cathodoluminescence

Cold cathodoluminescence observations at 2.5 \times , 4 \times and 10 \times magnifications were performed at the Department of Earth Sciences (University of Turin, Italy) with a microscope equipped with a CITL 8200 mk3 system. Operating conditions were 13–15 kV and 400 mA. Cathodoluminescence observations are essential for observing clinopyroxene zoning due to the very poor chemical zoning barely visible with BSE imaging (for further details, see [Ferrando et al., 2017](#)).

2.2. Microthermometry

Fluid inclusion microthermometry was carried out with a Linkam THMS600 heating/freezing stage, equipped with an Olympus BX60 (with 4 \times , 10 \times , 50 \times , long-distance focal length 100 \times magnifications), which operates in a temperature range between -196 and 600 °C at the University of Turin. The instrument was calibrated checking H₂O triple point (0.1 °C) in synthetic fluid inclusions (SYN-FLINC), with an accuracy of ± 0.2 °C. The phase transitions within fluid inclusions were measured with a heating rate varying from 1 to 5 °C/min. Compositions of analysed fluid inclusions, expressed as NaCl_{eq}, are calculated using the model of [Oakes et al. \(1990\)](#).

2.3. SEM-EDS and bulk-rock composition estimate

Whole section X-ray elemental maps were acquired using a scanning electron microscope (SEM-JEOL JSM-IT300LV), combined with an energy dispersive spectrometry (EDS) Energy 200 system and an SDD X-Act3 detector (Oxford Inca Energy), installed at the Department of Earth Sciences (University of Torino, Italy). The system is equipped with the Microanalysis Suite Oxford AZtecMineral and with the following analytical set up: an accelerating voltage of 15 kV, a counting time of 50 s, a processing time of 1 μ s, a working distance of 10 mm, magnification set at 50 \times and an estimated spatial resolution of 2.5 μ m/pixel. A high-resolution mineral modal map was elaborated using the ArcGIS[®]-based Quantitative X-ray Map Analyser (QXRMA) of [Ortolano et al. \(2018\)](#). This map was used to perform mass-balance calculations to obtain the bulk composition of the studied sample. Adopted mineral densities and compositions for mass-balance calculations are from [Deer et al. \(2013\)](#), and [Ferrando et al. \(2017\)](#), respectively, and are reported in [Supplementary Table 1](#) and [Supplementary Table 2](#), respectively.

In order to analyse opened fluid inclusions, five chips containing fluid inclusion-bearing crystals from a thick sec-

tion were frozen in liquid nitrogen, broken, and vertically mounted on a glass plate, and promptly carbon-coated. Examination of opened fluid inclusions and semi-quantitative determination of major elements of included minerals and globules of precipitated solutes were performed at the following operating conditions: low vacuum conditions (30 Pa) with an accelerating voltage of 15 kV, a counting time of 50 s, a processing time of 4 μ s, and a working distance of 10 mm. The data were acquired and processed using the Microanalysis Suite Issue 12, INCA Suite version 4.01.

2.4. Raman micro-spectroscopy

Raman spectra were acquired at the Department of Earth Sciences (University of Torino, Italy) using the confocal LABRAM HR800 (Horiba Jobin Yvon Instruments) of the Interdepartmental Center “G. Scansetti”, equipped with an Olympus BX41 microscope for transmitted and reflected light observations. Calibration was performed using the 521.6 cm⁻¹ Si, the 1331.8 cm⁻¹ diamond or the 2331.0 cm⁻¹ N₂ bands, depending on the spectral window considered during the analyses. Twenty-nine fluid inclusions in seventeen Cpx porphyroblasts have been selected and analysed. The identification of fluid and solid phases was based on the database of reference spectra of [Frezzotti et al. \(2012b\)](#). Operating conditions for both solids and fluids were: excitation line at 532 nm (solid-state Nd laser and 80 mW of emission power), edge filter, a grating of 600 grooves/mm, a confocal hole of 200 μ m, a slit from 40 to 200 μ m. The laser was focused on the sample using a 100 \times objective (laser spot of 1 μ m) for both solids and fluid phases. Each spectrum was collected by 2–5 accumulations of 5–60 s. Raman spectra baseline removal and fitting were performed with Fytik 1.3.1, and spectra fitting was performed with the built-in function Pearson7 for solid phases and with the built-in function PseudoVoight for fluids. Quantitative analyses on gaseous phases are obtained using the method described by [Burke \(2001\)](#).

2.5. Thermodynamic modelling

A Schreinemaker projection for the system CMS-H₂O-CO₂ ([Connolly and Trommsdorff 1991](#)) was constructed for conditions relevant for the BIU *P-T* path. It was calculated with the 6.8.9 version of the *Perple_X* software package ([Connolly, 1990](#)). The system CMS-H₂O-CO₂ was investigated using the thermodynamic database of [Holland and Powell \(2011 version DS6.22\)](#). The selected endmembers are: calcite, aragonite, dolomite, magnesite, forsterite, diopside, enstatite, quartz, coesite, tremolite, anthophyllite, lizardite, chrysotile, antigorite, brucite, A-Phase, clinohumite, chondrodite, and talc. The selected solution models are the calcite and dolomite model of [Anovitz and Essene \(1987\)](#) and the binary H₂O-CO₂ fluid model of [Connolly and Trommsdorff \(1991\)](#). For the H₂O-CO₂ fluid, the compensated Redlich-Kwong (CORK) equation of state (EoS) from [Holland and Powell \(1991\)](#) was applied.

A *P-T* isochemical phase diagram was obtained using the calculated DM675 S-bearing hydrous bulk-rock composition (i.e., CFMS-COHS system; see [Supplementary calculation 2.2](#)). The diagram was calculated with the “Lagged Speciation” algorithm ([Connolly and Galvez, 2018](#)) with condensed phase and molecular volatile species data from [Holland and Powell \(2011 version DS6.22\)](#) and solute species data from the DEW/HKF model of ([Sverjensky et al., 2014, revised 2017](#)). Data from the most recent revision of the DEW database ([Huang and Sverjensky, 2019](#)) was not employed because they lead to inconsistent results at low pressure (e.g., [Peng et al., 2020](#); [Macris et al., 2020](#)). The consequence of ignoring the species provided by [Huang and Sverjensky \(2019\)](#) is that the solute load estimated in the present work may be underestimated (especially in Mg). For the calculations, other mineral endmembers (pyrite, graphite, and diamond) and solution models (pyrrhotite, [Evans et al., 2010](#); antigorite, [Padrón-Navarta et al., 2013](#)) were added to the ones used for the Schreinemakers projection. The solvent consists of H₂O, CO₂, CH₄ and H₂S. The [Stern and Pitzer \(1994\)](#) EoS was used to describe pure H₂O and CO₂. All other pure fluid properties of the molecular species in the solvent were computed from the Modified Redlich-Kwong (MRK) of [De Santis et al. \(1974\)](#). All fluid species have been considered to model the fluid solute composition and speciation, except for the related molecular species already accounted for in the solvent (i.e., aqueous CO₂, aqueous CH₄ and aqueous H₂S). Cl and N₂, although relevant components of subduction fluids, have been excluded from the calculations for multiple reasons. The lack of constraints on the Cl and N₂ buffering capacity of chemical system (i.e., impossibility to reconstruct their contents in the same way as S, see [Supplementary Material 2.2](#)) implies that a completely arbitrary assumption on their content in the system has to be made. Although both have been detected in the residual fluid of analysed fluid inclusions, no representative value of their concentration in the originally trapped fluid can be retrieved. Moreover, in metamorphic rocks, Cl and N₂ are generally contained in phyllosilicates, but appropriate solution models are lacking, and adding Cl- and N₂-bearing end members to the thermodynamic calculations would require the use of representative fictive solid phases due to algorithmic requirements.

3. GEOLOGICAL SETTING

The well-known UHP Brossasco-Isasca Unit (BIU) of the Southern Dora-Maira Massif (Western Alps) is a continental Unit mainly composed of a Variscan amphibolite-facies metamorphic basement ([Compagnoni et al., 1995](#)) intruded by post-collisional Permian granitoids (ca 275 Ma, [Gebauer et al., 1997](#); [Compagnoni and Rolfo, 2003](#) and references therein), both reworked during Alpine subduction. The granitoids constitute the Monometamorphic Complex ([Fig. 1a](#)) that is now composed of metagranitoids, augen-gneiss, fine-grained orthogneiss, garnet + jadeite + kyanite + quartz granofels and the coesite-bearing pyrope whiteschist ([Chopin, 1984](#); [Compagnoni et al., 1995](#)). The Variscan metamorphic basement is

identified as the “Polymetamorphic Complex” ([Fig. 1a](#)) and comprises paraschists with widespread lenses and bodies of eclogites, marbles, and calc-silicate rocks. The Alpine *P-T-t*-d evolution of the BIU has been extensively investigated (e.g., [Castelli et al., 2014](#), [Ferrando et al., 2017](#); [Grosso et al., 2019](#) and reference therein); in [Fig. 1b](#), only the prograde and early-retrograde events relevant for this study are reported. A near-isothermal evolution from 450–570 °C and 1.0–1.8 GPa (1 in [Fig. 1b](#)) to 520–540 °C and 1.6–2.3 GPa (2 in [Fig. 1b](#); [Grosso et al., 2019](#)) can be observed during the early prograde evolution. The development of the prograde (now relict) foliation likely occurred at the HP-UHP transition (at ca. 557 °C and ca. 2.7 GPa; [Ferrando et al., 2017](#); [Grosso et al., 2019](#)) at 41–35 Ma ([Gebauer et al. 1997](#); [Di Vincenzo et al., 2006](#); [Gauthiez-Putallaz et al., 2016](#)). The UHP metamorphic peak at ca. 4.3 GPa and ca. 730 °C ([Castelli et al., 2007](#) and references therein; [Ferrando et al., 2009](#) and references therein) was reached at 35 Ma (4 in [Fig. 1b](#); [Rubatto and Hermann, 2001](#)). The regional foliation developed during early exhumation, still at UHP condition (5 in [Fig. 1b](#); ca. 3.7–4.0 GPa and ca. 720–740 °C; [Ferrando et al., 2009](#)). In the largest marble lens of Costa Monforte, [Ferrando et al. \(2017\)](#) found evidence of multiple carbonate dissolution and reprecipitation events during the prograde to early-retrograde stages (dashed yellow line in [Fig. 1b](#)). This process occurred in the presence of an aqueous solute-bearing COH fluid produced by prograde dehydration, where the CO₃²⁻ component was thermodynamically modelled at 0.03–0.08 mol% of CO₂ by classical molecular-fluid thermodynamics. The presence of solutes in the UHP fluid was inferred from qualitative data on fluid inclusions in clinopyroxene ([Ferrando et al., 2017](#)).

4. PETROGRAPHY AND FLUID INCLUSION DATA

4.1. Sample petrography

The selected polymetamorphic mm-banded marble (sample DM675; [Fig. 2a, b](#); [Ferrando et al., 2017](#)) is an impure calcitic-dolomitic marble belonging to the chemically simple C(F)MS-COH system and consisting of calcite (after former HP/UHP aragonite), dolomite, clinopyroxene (diopside), olivine (Mg-rich), rare accessory apatite and phlogopite, and retrograde serpentine ([Fig. 2a](#)). Dolomite occurs as large-grained porphyroblasts, whereas both olivine and clinopyroxene are present as medium-grained porphyroblasts and fine-grained neoblasts. Medium- to fine-grained recrystallised calcite constitutes the matrix between and within Cpx-rich and Cpx + Ol + Dol layers (mineral abbreviations from [Whitney and Evans, 2010](#)), each of them being composed of variable modal amounts of the minerals mentioned above. Based on cathodoluminescence observations and mineral-chemical composition, distinct generations are observed in zoned clinopyroxene ([Fig. 2c, d, g](#)).

Prograde-to-peak primary (i.e., trapped during host growth; [Roedder, 1984](#)) FIs occur only in clinopyroxene belonging to the clinopyroxene-rich layer ([Fig. 2a, b](#)), and not in other prograde-to peak minerals. Therefore, cathodoluminescence observations and mineral-chemical

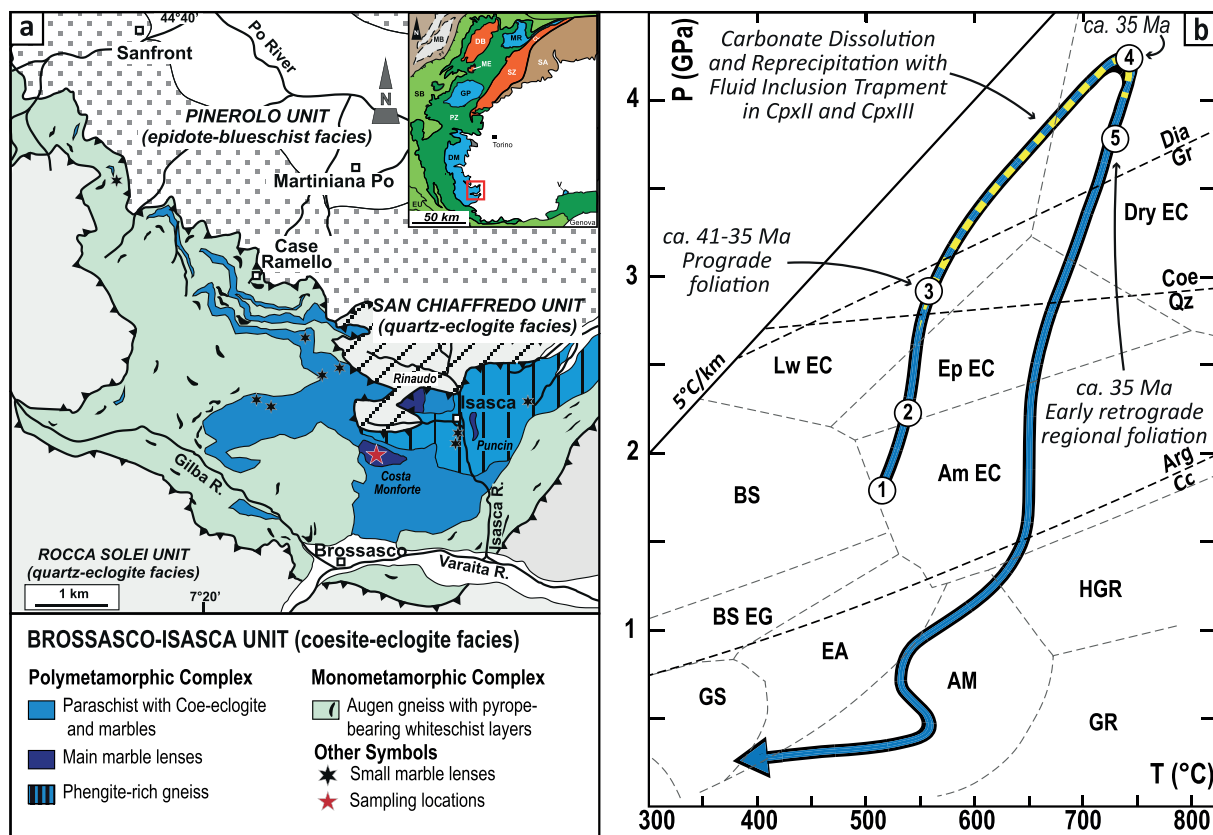


Fig. 1. (a) Simplified geologic map of the Brossasco-Isasca Unit modified from Ferrando et al. (2017). The inset shows the position of the Southern Dora-Maira Massif within a simplified tectonic map of the Western Alps. Helvetic-Dauphinois domain: MB = Mont Blanc-Aiguilles-Rouges. Penninic domain: SB = Grand St. Bernard Zone; MR = Monte Rosa; GP = Gran Paradiso; DM = Dora-Maira; V = Valosio; PZ = Piemonte zone of calcschists with meta-ophiolites. Austroalpine Domain: DB = Dent Blanche nappe; ME = Monte Emilius klippe; SZ = Sesia-Lanzo zone; SA = Southern Alps; EU = Embrunais-Ubaye flysch nappe; PF = Penninic thrust front; CL = Canavese line. (b) Alpine P-T-t-d path of the Brossasco-Isasca Unit inferred from previous studies (prograde path: Groppo et al., 2019; peak and retrograde path: from Ferrando et al., 2017 and references therein). The dashed yellow line indicates the P-T interval in which Ferrando et al. (2017) inferred the occurrence of carbonate dissolution and reprecipitation. (For interpretation of the references to colour in this figure legend, the reader is referred to the web version of this article.)

data are reported only for clinopyroxene (for a more complete petrographic and mineral-chemical description of the sample DM675 see Ferrando et al., 2017). Clinopyroxene is nearly pure diopside and occurs both as large subhedral to euhedral porphyroblasts, roughly defining the early-retrograde regional foliation, and as small euhedral neoblasts (Fig. 2a, b, d). Cathodoluminescence observations reveal an irregular but sharp zoning (corroded and lobate) characterising both porphyroblasts and neoblasts. This cathodoluminescence (CL) zoning is related to a less evident major-element chemical zoning (Fig. 2d; Fig. 3a, c, e). Based on data from Ferrando et al. (2017), combined with new observations (i.e., Cpx VI, presented at the end of this paragraph), the following six generations of clinopyroxene can be recognised (Fig. 2c, d). Cpx I corresponds to the rare pre-Alpine core of porphyroblasts, and it is characterised by non-luminescent brown colour, high Mg content (ca. 0.946 a.p.f.u.), and the highest Fe and Na contents (0.042 a.p.f.u. and 0.010 a.p.f.u., respectively) among all the Cpx generations. Cpx II, representing the HP-UHP prograde generation, shows a dark-yellow colour in CL,

and locally includes irregular reddish Dol or orange-to-brown Mg-Cal crystals. It has higher Mg (0.987–1.010 a.p.f.u.) and lower Fe, and Na (0.011–0.019 a.p.f.u. and 0.004–0.006 a.p.f.u., respectively) contents than Cpx I. Cpx I and Cpx II are generally well observable in the medium-grained porphyroblast, while they tend to be rather small (and rarer) in the neoblasts. Cpx III represents the UHP metamorphic peak and shows the brightest yellow cathodoluminescence colours observable in the sample. It is pure diopside with the highest Mg (0.987–1.010 a.p.f.u.) the lowest Fe (0.001–0.008 a.p.f.u.) contents and Na content below the detection limit. Cpx IV represents the early-retrograde UHP generation. It has a cathodoluminescence colour similar to that of Cpx II, but it irregularly grows after Cpx III (Fig. 2d, e; Fig. 3a). Cpx IV is chemically similar to Cpx III (i.e., Mg = 0.991–1.000 a.p.f.u., Fe = 0.006–0.009 a.p.f.u. and Na = 0.004 a.p.f.u.). In most cases, these four generations constitute at least 80–90 vol% of each clinopyroxene crystal. Generally, the euhedral habit of Di crystals in DM675 is due to the last two thin retrograde stages of growth. Cpx V and Cpx VI (Fig. 2d, Fig. 3a, c,

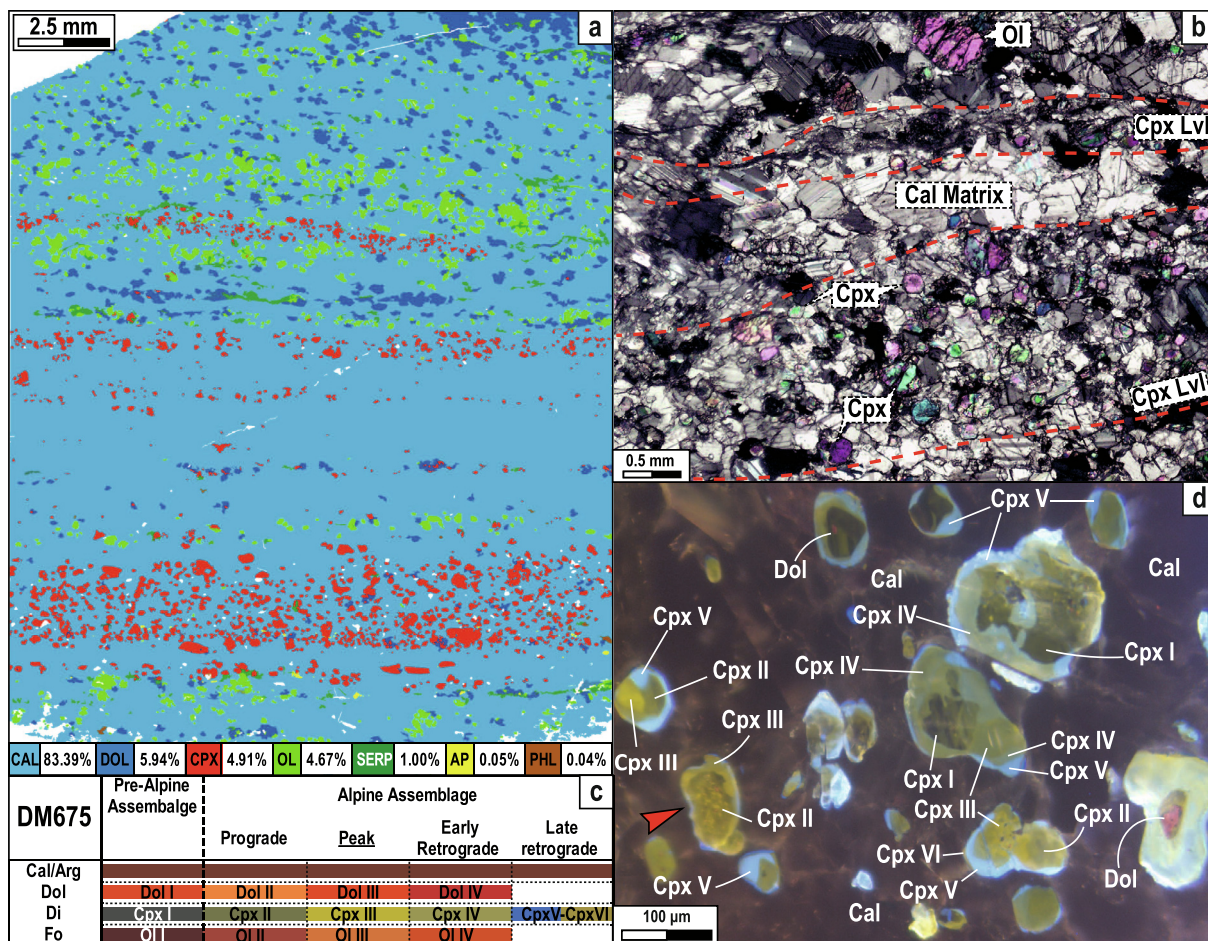


Fig. 2. (a) Modal map of sample DM675 obtained by processing the X-ray elemental maps. (b) Crossed-polarised light (XPL) photomicrograph of the studied marble. Its typical banding is defined by variations in grain size and/or modal composition (Clinopyroxene level: Cpx Lvl). (c) Metamorphic evolution of DM675 (modified from Ferrando et al., 2017). The colours of each mineral and their generations match the cathodoluminescence (CL) palette. (d) Cathodoluminescence photomicrograph showing the typical microstructural relationships between the different Cpx generations. The bright spots within Cpx II (where present) are fluid inclusions close to the sample surface (red arrow). (For interpretation of the references to colour in this figure legend, the reader is referred to the web version of this article.)

e) are characterised by an intense blue to light-blue and dark-yellow luminescence, respectively. In retrograde Cpx, Mg content is lower (0.990–0.995 a.p.f.u.) than in the UHP Cpx, Fe is among the highest (0.002–0.011 a.p.f.u.) and Na content is low (0.002–0.003 a.p.f.u.). Due to the lack of metamorphic reactions (Supplementary Fig. 4) from the peak down to the aragonite to calcite transition, Cpx-V-VI formed during and after this transition occurred, respectively.

4.2. Fluid and solid inclusion petrography

Detailed petrographic investigation (Figs. 3–4) distinguishes four main groups of synchronous inclusions (Touret, 2001) within zoned porphyroblastic diopside (i.e., Type I, II, III and IV). The primary Type I fluid inclusions will be designated as Early Type I, while the secondary Type II, III and IV will be regarded as Late Type. Early Type I fluid inclusions are present only as primary inclusions within prograde-to-peak clinopyroxene (i.e., Cpx II

and Cpx III). In contrast, Late Type fluid inclusions constitute secondary intragranular trails, grain-boundary to interior and grain-boundary to grain-boundary depending on the dimensions of host clinopyroxene, that cut through Cpx V and VI (Fig. 3c, d, e). This microstructural evidence constrains their entrapment during the late retrograde stages. Because the fluid trapped in Late Type fluid inclusions represents the fluid circulating during exhumation, they are not further considered in this work (for further petrographic details on Late Type fluid inclusions and their inferred trapping conditions, see Supplementary Material 3).

In contrast, because Early Type I fluid inclusions represent the fluid circulating at HP-UHP conditions, they have been further investigated by microthermometry, Raman micro-spectroscopy and SEM-EDS (Figs. 5–6). Early Type I (Fig. 3b, Fig. 4) fluid inclusions are variable-sized (5–25 μm), primary tri-phase multi-solid aqueous inclusions (different kinds of solids + liquid + vapour), grouped in clusters at the core of prograde and peak Di

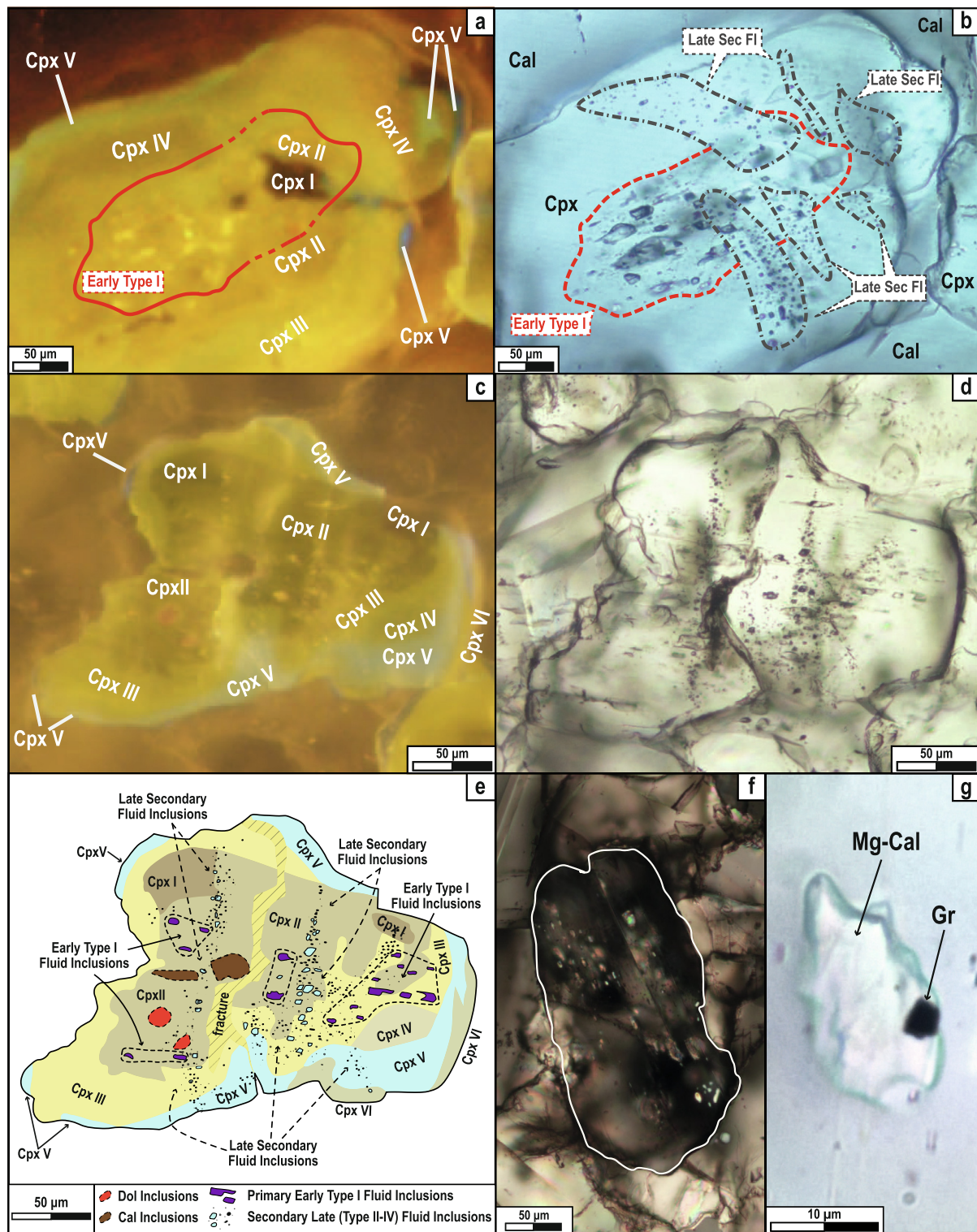


Fig. 3. (a-b) Cathodoluminescence (a) and PPL (b) photomicrographs showing the microstructural relationships between Cpx generations and fluid inclusion Types. (c-d-e) Cathodoluminescence (c), PPL (d) and a comprehensive sketch (e) of a Cpx crystal characterised by all the six Cpx generations. The microstructural relationships between Early Type I fluid inclusions, Late secondary fluid inclusions, carbonate inclusions and mineral zoning are outlined. Note that Early Type I fluid inclusions are present only in Cpx II and Cpx III, whereas Late secondary fluid inclusions crosscut all Cpx generations. Solid carbonate inclusions (either dolomite and calcite) are included in Cpx II. (f) Crossed-polarised photomicrograph of a fluid inclusion-bearing Cpx showing how fluid inclusions are marked by the high interference colours of included mineral phases. (g) Detail of a solid inclusion of carbonate with a graphite flake at the contact with the host Cpx II (PPL).

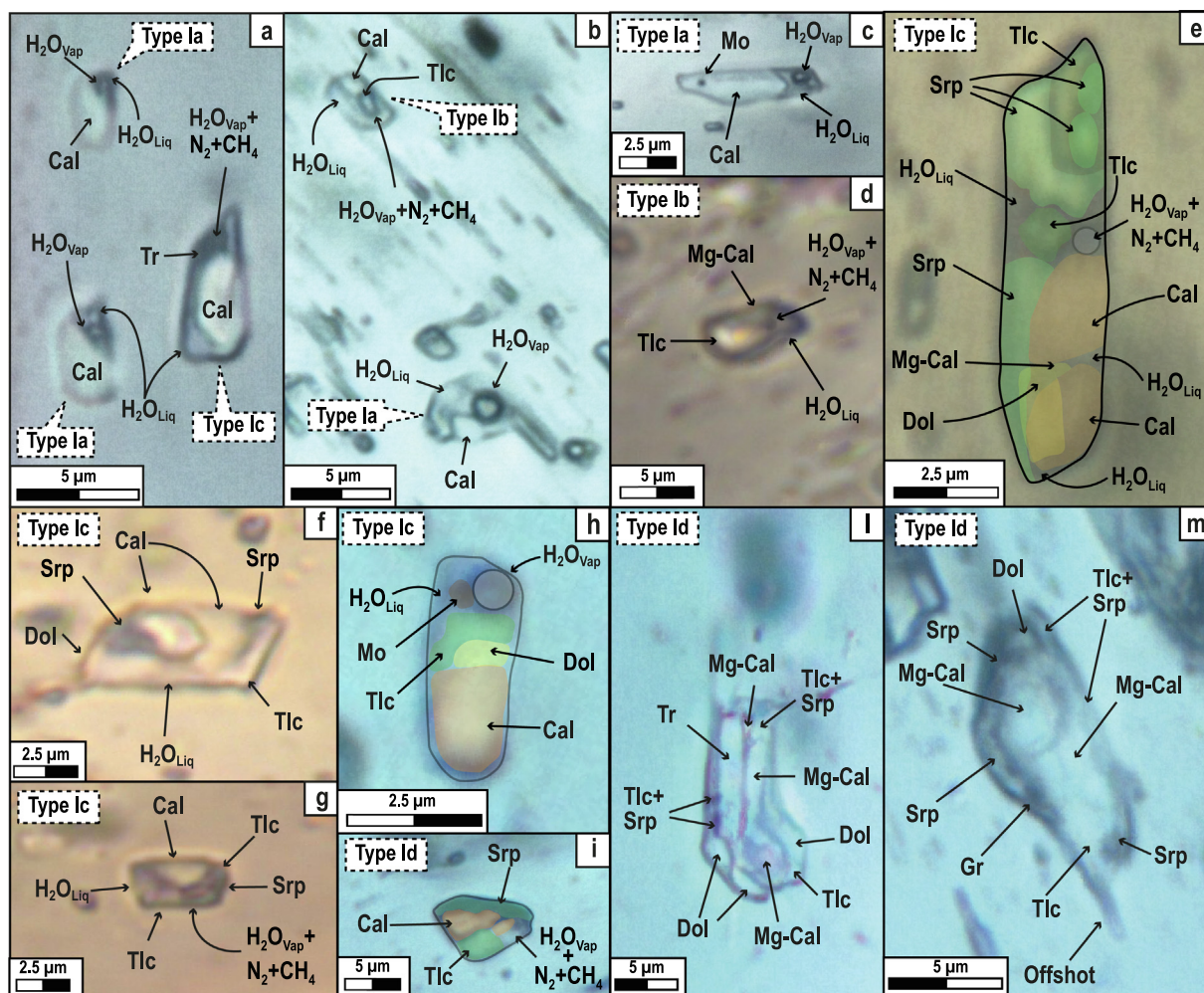


Fig. 4. (a–m) Stacked photomicrographs (PPL) of Early Type I FI showing their habit, fluid/solid ratios, type of solids and other relevant microstructures (i.e., offshoots). (e), (h) and (i) are overlaid by sketches (i.e., image overlays drawn by hand) of their fillings; note the 3D overlapping of mineral phases in (e) (i.e., Dol below Srp and Cal).

(Cpx II – Cpx III) and can be easily spotted due to the abundance of birefringent crystals within them (Fig. 3f). Typically, these inclusions have negative-crystal shapes, but the largest inclusions often present offshoots near the cleavage of the host clinopyroxene. The volume proportions of the phases in the inclusions, have been estimated by combining image analysis and Raman data of 29 Early Type I inclusions (Table 1; see Supplementary calculation 2.1). Early Type I fluid inclusions can be further subdivided combining: (i) habit and dimension (i.e., negative crystal shape vs irregular with offshoots, small vs big); (ii) number and kind of solids within each fluid inclusions; (iii) volumetric proportion filled by solids of each fluid inclusion; (iv) predominance of liquid vs vapour fluid phase filling the mineral interstices. Based on these characteristics, four sub-Type I fluid inclusions can be distinguished (Table 1):

- o Type Ia: 3–8 μm sized inclusions (Fig. 4a–c) showing negative-crystal shape or, locally, irregular contours. They usually contain a single, large, birefringent crystal of calcite (up to 83 vol%; Fig. 3f; 4a; 5a), $\text{H}_2\text{O}_{\text{Liq}}$ fills

the remaining volume (down to 15 vol%; Fig. 5h) and $\text{H}_2\text{O}_{\text{vap}}$ ($\sim <0.5\text{--}8$ vol%, Fig. 5g) phases. Their solid/fluid ratio (defined as [solid vol/(solid vol + liquid vol + vapour vol + empty vol)]; Table 1) is highly variable, ranging from 0.16 to 0.81. Rarely, a small opaque mineral also occurs (Fig. 4c). Raman and SEM-EDS analyses reveal the presence of chalcopyrite-like and molybdenite-like sulphide minerals (Fig. 5i–j).

- o Type Ib: 3–6 μm sized fluid-rich inclusions (Fig. 4b, d) with negative-crystal shape filled by $\text{H}_2\text{O}_{\text{Liq}}$ ($\sim 69\text{--}75$ vol%; Fig. 5d, h), two tiny rounded birefringent crystals ($\sim 22\text{--}29$ vol%; calcite or Mg-calcite and talc; Fig. 4b, d, 5a–b, d) and a vapour bubble ($\sim 2\text{--}3$ vol%) composed by a mixture of $\text{H}_2\text{O}_{\text{vap}} \pm \text{N}_2 \pm \text{CH}_4$ (with 97–98 mol% of N_2 and 3–2 mol% of CH_4 ; Fig. 5g). Their solid/fluid ratio ranges in a small interval from 0.16 to 0.22 (Table 1).
- o Type Ic: 4–15 μm sized crystal-rich inclusions (Fig. 4a, e–h) showing negative-crystal shape or, locally, irregular contours and offshoots. They are characterised by multiple variable-sized birefringent crystals ($\sim 50\text{--}90$ vol%)

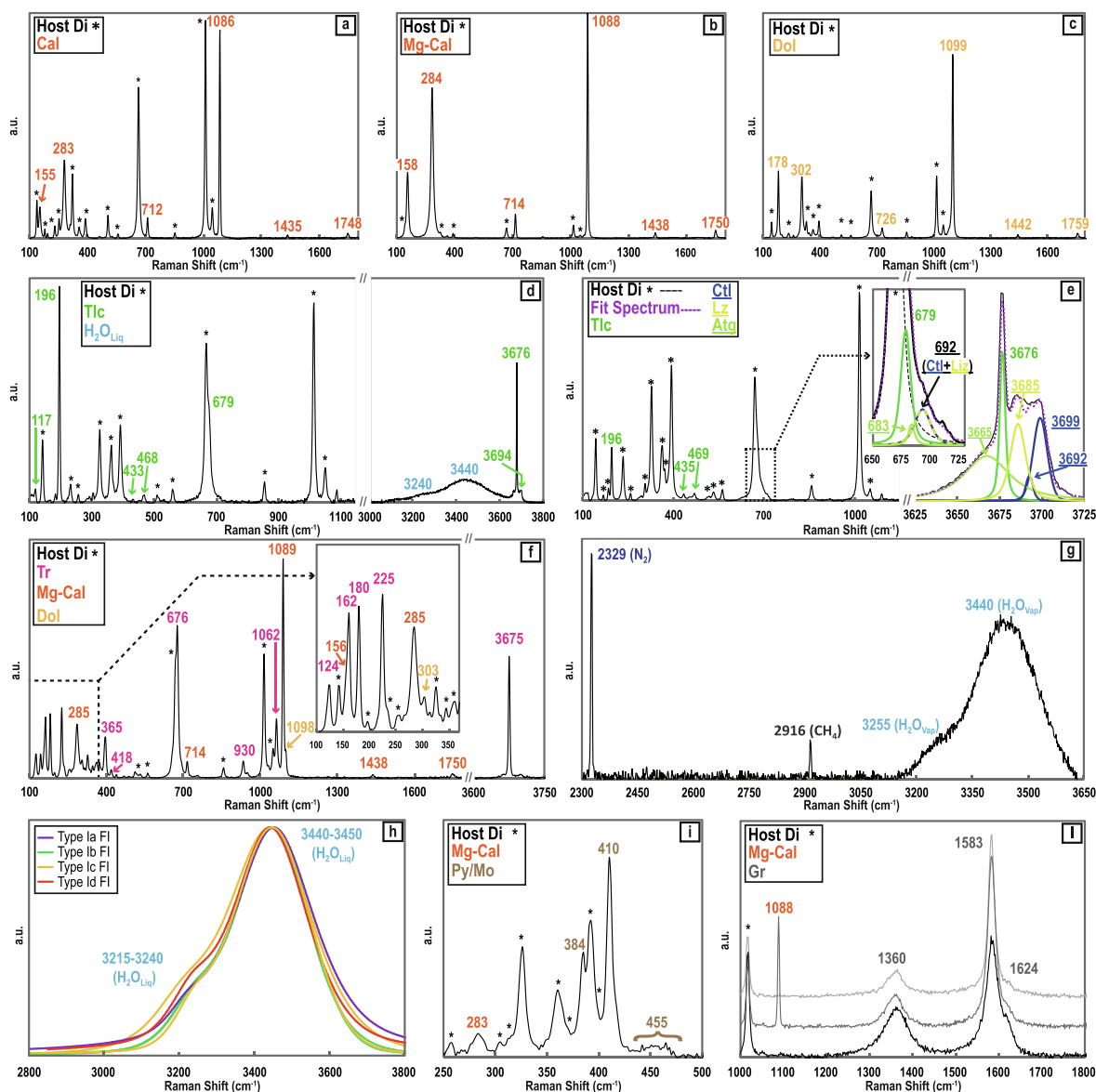


Fig. 5. Representative single (a–c, h) and mixed (d–g, i–l) Raman spectra of mineral (a–f, i–l) and fluid phases (d, g, h) observed in Early Type I fluid inclusions. (h) $\text{H}_2\text{O}_{\text{Liq}}$ Raman bands for Early Type I fluid inclusions (thick colour-coded lines). A distinct vertical scale is used in each figure to make readable the spectra.

and a highly variable solid/fluid ratio (0.52–0.91, Table 1). Calcite and Mg-calcite are the dominant carbonates (Fig. 4a, e–h), while dolomite is always subordinate (Fig. 4–e–f, h; Fig. 5c). Among the hydrous silicates, talc is always present, serpentine is common, and tremolite is rare (Fig. 4a, e–h; Fig. 5d, e–f). The Raman shape of the OH bands of serpentine reveal the presence of at least two or all the three serpentine polymorphs (Fig. 5e; Petriglieri et al., 2015; Tarling et al., 2018). In most cases, a mixed talc + serpentine spectrum is obtained from lamellar crystals (Fig. 5e). Small opaque minerals, identified as sulphides (see Type Ia fluid inclusions), are locally observed (Fig. 4h). Raman investigation reveals the presence of

interstitial saline liquid $\text{H}_2\text{O}_{\text{Liq}}$ (~8–48 vol%), whereas the bubble (~1–30 vol%) consists of $\text{H}_2\text{O}_{\text{Vap}} \pm \text{N}_2 \pm \text{CH}_4$ (Fig. 4a, e–h).

- o Type Id: up to 25 μm sized multiphase-solid inclusions (Fig. 4i–m), with irregular contours and offshoots, filled by 5–12 crystals of variable size and variable volumetric proportions. The range of solid/fluid ratio ranges in a relatively small interval and shows the highest values (0.86–1.0; Table 1) of all the sub-types. Carbonates (mainly Mg-calcite, calcite, and dolomite) are dominant. Tremolite and serpentine are the main hydrous silicate phases, followed by talc, usually mixed with serpentine. Notably, serpentine minerals tend to be located on the

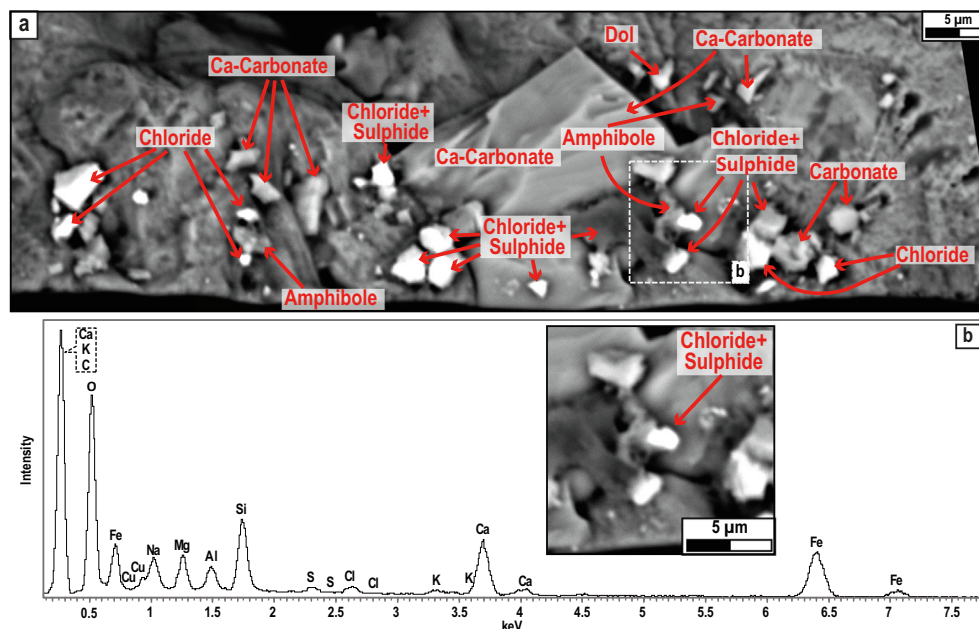


Fig. 6. (a) BSE image of opened fluid inclusions from a broken chip. Silicates and carbonates are interpreted as formerly included solid phases, while the sulphide and chloride globules are interpreted to be precipitated from the former liquid water filling the inclusions. (b) Qualitative EDS chemical analysis of the minerals precipitated by the liquid phase (inset image) and of the hosting clinopyroxene.

inclusion's walls in contact with host clinopyroxene (Fig. 4i–m). The rare opaque minerals are sulphides (see Type Ia and Ic fluid inclusions) and graphite in only one case (Fig. 5l). The interstitial space (<20 vol%) can be either empty or filled with $\text{H}_2\text{O}_{\text{Liq}}$ or $\text{H}_2\text{O}_{\text{Vap}}$ or with a gas mixture ($\text{H}_2\text{O}_{\text{Vap}} \pm \text{N}_2 \pm \text{CH}_4$).

Prograde Cpx II and peak Cpx III locally include solid inclusions of dolomite and Mg-calcite randomly distributed near Early Type I inclusions (Fig. 3c–e). Their size varies from 10 to 50 μm , and their shape is from sub-spherical to amoeboid with irregular or smooth contours. Locally, a graphite flake (confirmed by Raman analysis) occurs at the contact between the host clinopyroxene and the carbonate inclusion (Fig. 3g).

4.3. Composition of UHP fluid inclusions

Microthermometric measurements on Early Type I fluid inclusions in which phase transitions are recognisable are characterised by the first evidence of melting between $-49.9\text{ }^\circ\text{C}$ and at $-43\text{ }^\circ\text{C}$. Because of the difficulty of observing because it is difficult to observe the first melting, due to the high volume of solids, these temperatures likely represent an extensive melting of antarctite, indicating the presence of dissolved CaCl_2 , possibly in addition to NaCl , within $\text{H}_2\text{O}_{\text{Liq}}$. The final melting of ice is at $-14.5\text{ }^\circ\text{C}$ in one Type Ic FIs, and between -6.7 and $-6.3\text{ }^\circ\text{C}$ in three Type Ia FIs. These final melting temperatures correspond to salinities of 18.1 wt% and 10.3–9.8 wt% in NaCl_{eq} , respectively.

SEM-EDS qualitative analyses of opened fluid inclusions (Fig. 6a) confirm the local occurrence of Cl–Na–K pre-

cipitates (Fig. 6a), indicating the presence KCl, in addition to NaCl and CaCl_2 , as dissolved chlorides (Fig. 6b). Finally, a local occurrence of Fe–Cu–S precipitates (chalcopyrite-like minerals Fig. 6b), coupled with Raman evidence of sulphide minerals (Fig. 5i), indicates the presence of S, Fe, Cu and Mo within the trapped fluid.

Fluid inclusion image analysis combined with Raman data, and microthermometric data, when available, allowed mass balance calculations of the included minerals and fluids, leading to the reconstruction of the bulk composition (expressed as mol% of single elements instead of the classical wt% of oxides, for convenience with the used algorithms in both mass balance and thermodynamic calculations) of 29 Early Type I fluid inclusions (Table 1; for all the details regarding the calculations see Supplementary Material 2.1). The fluid composition reconstructed from Type Ia fluid inclusions is characterised by variable, but sometimes remarkably high, H_2 (9.5–57.0 mol%), C (4.3–24.1 mol%) and Ca (3.9–22.9 mol%) contents. Where measured, Cl and S_2 are minor components, with Cl ranging from 0.3 and 0.6 mol% and S_2 totalling 0.2 mol% (Table 1). The fluid chemistry in Type Ib (Table 1) is quite homogeneous and characterised by the highest H_2 content (49.3–53.0 mol%) among all Type I fluid inclusion and by relatively low C, Ca, Si, and Mg contents (4.3–4.4 mol%; 3.9–4.0 mol%; 1.8–3.6 mol% and 1.4–2.8 mol% respectively). The fluid in Type Ic is less H_2 -rich (12.3–39.9 mol%) and more C-rich (10.2–18.7 mol%) than Type Ib, while the other non-volatile elements show higher concentration than in Type Ib fluid inclusions (Si = 1.9–11.5 mol%; Mg = 1.5–13.5 mol%; Ca = 9.4–17.1 mol%). When sulphide is detected, the S_2 content in the reconstructed fluid reaches 1.2 mol%. Similarly, where the fluid salinity has been measured,

the corresponding Cl content is 0.3 mol% (Table 1). The fluid in Type Id fluid inclusions (Table 1) has the lowest H₂ content (3–21.9 mol%) and the highest cation content among all Type I fluid inclusions (Si = 5.8–14.7 mol%; Mg = 6.4–14.4 mol%; Ca = 10–19.9 mol%; C = 11.0–21.9 mol%). S₂, where measured, is the highest among all Type I fluid inclusions, varying from 1.4 to 2.0 mol% (Table 1).

These variations in chemical composition raise the question of the typology and the extent of the post-entrapment chemical modifications experienced by every single inclusion and on the preservation of the chemical composition of the trapped fluid.

5. THERMODYNAMIC CALCULATIONS

5.1. Petrogenetic grid of the system diopside-molecular fluid

Because HP-UHP fluid inclusions may experience post-entrapment chemical modifications due to fluid-host interactions, a Schreinemaker projection in the simplified CMS-H₂O-CO₂ (Ca-Mg-Si-H₂O-CO₂) system has been computed to identify the possible reactions involving the diopside, the FI host of interest, and a binary H₂O-CO₂ fluid. We use this simplified molecular-fluid model because it has been shown elsewhere that the solute chemistry of the fluid has little influence on mineral stability (Galvez et al., 2015, 2016; compare Supplementary Fig. 3 and Supplementary Fig. 4).

To reproduce the minerals observed within Early Type I FI, we focussed on reactions such as:



where Di represents the host diopside, F is an H₂O-CO₂ fluid mixture, and “other minerals” qualitatively represent the related additional components dissolved in the fluid (i.e., Si, C, Ca, and Mg; see inset in Fig. 7). Since such reactions most likely occurred during exhumation stages, we consider only univariant equilibria in which Di + F react with decreasing temperature (thick green lines; Fig. 7). Equilibria that fulfil these requirements can produce Arg (Cal), Dol, Mg-Cal, Tlc, Tr, and Atg in various combinations.

The post-entrapment reactions in the host diopside-trapped fluid system are characterised by a steep negative Clapeyron slope that orients them nearly perpendicularly to the slope of the fluid isochores (Figs. 7, 8). For this reason, the temperature of the system has more impact on the type of post-trapping reactions than the pressure.

5.2. Thermodynamic modelling of the peak minerals-electrolytic fluid assemblage

In order to verify that the Early Type I fluid inclusions preserve the chemical composition of the formerly trapped fluid, the metamorphic evolution of the fluid phase in equilibrium with the mineral assemblage of sample DM675 along the prograde BIU *PT*-path has been modelled by electrolytic-fluid thermodynamics (Supplementary Fig. 4). To do this, the S-bearing (due to the presence of sulphides within Type I FI; see Supplementary Calculation 2.2)

hydrous bulk-rock composition of the sample corresponding to DM675 (i.e., CFMS-COHS system) before prograde dehydration has occurred was reconstructed as described in the Supplementary Material (see Supplementary calculation 2.2 and Supplementary Table 3). The results of the modelling show that at the UHP peak, the mineral assemblage consists of aragonite, olivine, clinopyroxene, fluid, dolomite, pyrite, diamond and clinohumite (Table 2). Up to 96.39 mol% of the fluid in equilibrium with this mineral assemblage consists of a H₂O + CO₂ + CH₄ + H₂S mixture, while the remaining 3.61 mol% is constituted by neutral and charged species of Si, Ca, Mg, Fe, C and S₂ (Table 2).

6. DISCUSSION

6.1. Post-entrapment chemical modifications predicted by molecular fluid thermodynamics

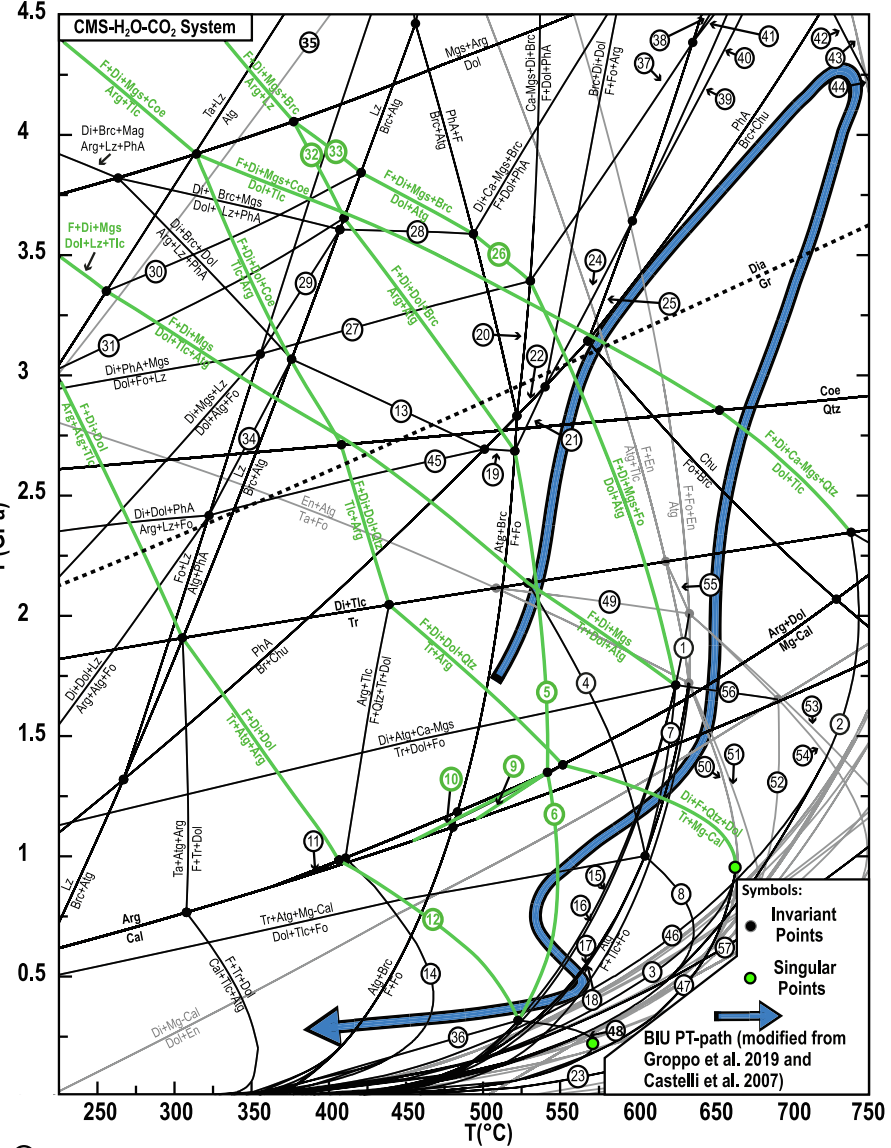
The reactions capable of producing the minerals observed within Early Type I fluid inclusions are depicted in the general petrogenetic grid of Fig. 7 and have been isolated in Fig. 8. In order to better identify the possible post-entrapment reactions, the fluid isochores (dashed grey lines in Fig. 8) are also depicted because they represent the most likely *P-T* paths followed by the fluid inclusions during exhumation (e.g., Touret, 2001). The isochore at 1.3 g/cm³ (the orange dashed line in Fig. 8) is the fluid isochore that crosscuts the *P-T* conditions of the BIU metamorphic peak. This isochore represents the maximum density reached by the fluid during its entrapment (i.e., maximum trapping isochore; cf. Supplementary Material 1.1) and also defines the upper limit of the *P-T* conditions followed by fluid inclusions during their exhumation path (see more information regarding the isochoric decompression path in the Supplementary Material 1.1). Due to the lack of reliable constraints on the original salinity and N₂ content of the trapped fluid, halogens and N₂ have been excluded from the fluid isochore calculation and the thermodynamic modelling of the peak fluid. The expected changes in the slopes of the isochores resulting from the addition of salts would not influence the type of post-entrapment reactions. The reactions (with the corresponding *P-T* range of occurrence) have also been summarised in Table 3.

Starting from Type Ia fluid inclusions, the lack of a post-trapping reaction able to reproduce only a single calcite/aragonite crystal (i.e., Arg as the only reaction product in Table 3 and Figs. 7, 8) excludes that it is a step-daughter mineral. It is not considered a daughter mineral because of its very high-volume proportion (up to 83.3 vol% of the fluid inclusion). For these reasons, the single large crystal of calcite typical of these inclusions is interpreted as an incidentally-trapped mineral. The main implication is that the UHP fluid was a CaCO₃-oversaturated fluid already precipitating aragonite in the rock matrix during the entrapment. This also suggests that the bulk composition of Early Type I fluid inclusions could randomly overestimate the Ca- and C-content.

Five representative Type Ib, Ic, and Id fluid inclusions are reported in Fig. 8 to illustrate the subsequent steps of

Reactions:

- ① $Tr+Dol+Fo = F+Di+Mgs$
- ② $Tlc+Dol = Qtz+Tr+F+Ca-Mgs$
- ③ $Tr+Qtz+Mg-Cal = F+Di+Dol$
- ④ $Dol+Tlc+Atg = F+Tr+Ca-Mgs$
- ⑤ $Arg+Atg = F+Di+Dol+Fo$
- ⑥ $Atg+Mg-Cal = F+Di+Fo+Dol$
- ⑦ $Dol+Atg = F+Tr+Fo+Ca-Mgs$
- ⑧ $Dol+Fo+Tlc = F+Tr+Mgs$
- ⑨ $Atg+Arg = F+Fo+Di+Mg-Cal$
- ⑩ $Tr+Arg = F+Qtz+Di+Mg-Cal$
- ⑪ $Tlc+Arg = F+Qtz+Tr+Mg-Cal$
- ⑫ $Cal+Tr+Atg = F+Di+Dol$
- ⑬ $Arag+Atg+PhA = Dol+Di+Brc$
- ⑭ $Mg-Cc+Tlc = F+Qtz+Tr+Dol$
- ⑮ $Di+Dol+Atg = F+Tr+Fo$
- ⑯ $Di+Atg = F+Tr+Fo$
- ⑰ $Atg+Mag = F+Tlc+Fo$
- ⑱ $Dol+Atg = F+Tlc+Fo+Tr$
- ⑲ $Fo+Arg+Atg = Di+Brc+Dol$
- ⑳ $Atg+PhA = F+Fo$
- ㉑ $Di+Brc+Di = F+Fo+Arag$
- ㉒ $PhA = Brc+Fo$
- ㉓ $Di+Dol = F+Fo+Mg-Cal$
- ㉔ $Dol+Di+PhA = F+Arag+Fo$
- ㉕ $Fo+A-Phase = Chu$
- ㉖ $Dol+Atg = F+Di+Ca-Mgs+PhA$
- ㉗ $Atg+PhA = Fo+F$
- ㉘ $Dol+Atg+PhA = Di+Brc+Mgs$
- ㉙ $Di+Mgs+Lz = Dol+Atg+PhA$
- ㉚ $F+Di+Lz+Mag = Dol+Atg$
- ㉛ $Tlc+Mag+Fo = En + F$
- ㉜ $Arg+Lz = F+Dol+Di+Br$
- ㉝ $Dol+Tlc = F+Di+Coe$
- ㉞ $Dol+Di+Lz = Arg+Atg+PhA$
- ㉟ $En+Lz = Atg+Fo$
- ㊱ $Dol+Atg+Di = Mg-Cal+Tr+Fo$
- ㊲ $Di+Ca-Mgs+PhA = F+Dol+Fo$
- ㊳ $Di+Ca-Mgs+PhA = F+Dol+Chu$
- ㊴ $Dol+Di+PhA = F+Chu+Arag$
- ㊵ $Dol+Atg = F+Ta+Fo+Tr$
- ㊶ $Di+Ca-Mgs+Chu = F+Dol+Fo$
- ㊷ $Chu+Brc = Chn$
- ㊸ $Tlc+Mgs = F+Coe+En$
- ㊹ $Tlc = F+Coe+En$
- ㊺ $Di+Dol+PhA = Atg+Fo+Arag$
- ㊻ $Ta+Qtz+Dol = Tr+F+Mg-Cal$
- ㊼ $Dol+Tlc = Tr+Mg-Cal+Fo+F$
- ㊽ $Tlc+Atg+Arg = F+Dol+Tr$
- ㊾ $Tr+Fo = Atg+En+Di$
- ㊿ $Tlc+Mg-Cal+Fo = En+ F$
- ① $Tlc+Fo = F+En$
- ② $Tr+Mg-Cal+Fo = Dol+En+F$



- ③ $Tr+Fo = F+Di+En$
 - ④ $Dol+Tr+Fo = Di+En+F$
 - ⑤ $Tr+Atg = F+Di+En$
 - ⑥ $Mg-Cal+Tlc = F+Qtz+Tr+Dol$
 - ⑦ $Qtz+Dol = F+Di$ & $Tr+Qtz+Dol = F+Mg-Cal$
- Reactions colour-code:
 Reactions able to produce the observed minerals included in FI during exhumation
 Reactions with mineral phases "seen" by the sample (i.e. in the pseudosection)
 Reactions with mineral phases "not seen" by the sample (i.e. in the pseudosection)

Structure of reactions able to produce the observed minerals included in FI during exhumation

REPRESENTATIVE OF THE ELEMENTS DISSOLVED IN THE FLUID (i.e. Ca, Si, Fe, C)

$Di + F + \text{Other Minerals} \rightarrow \text{Step-Daughter Minerals}$

H_2O+CO_2

HT ←→ LT

Fig. 7. Complete mixed-volatile molecular-fluid Schreinemakers projection (Connolly and Trommsdorff 1991) for conditions relevant for the BIU path and covering the P-T range on interest for the evaluation of chemical interactions between the host clinopyroxene and the molecular fluid.

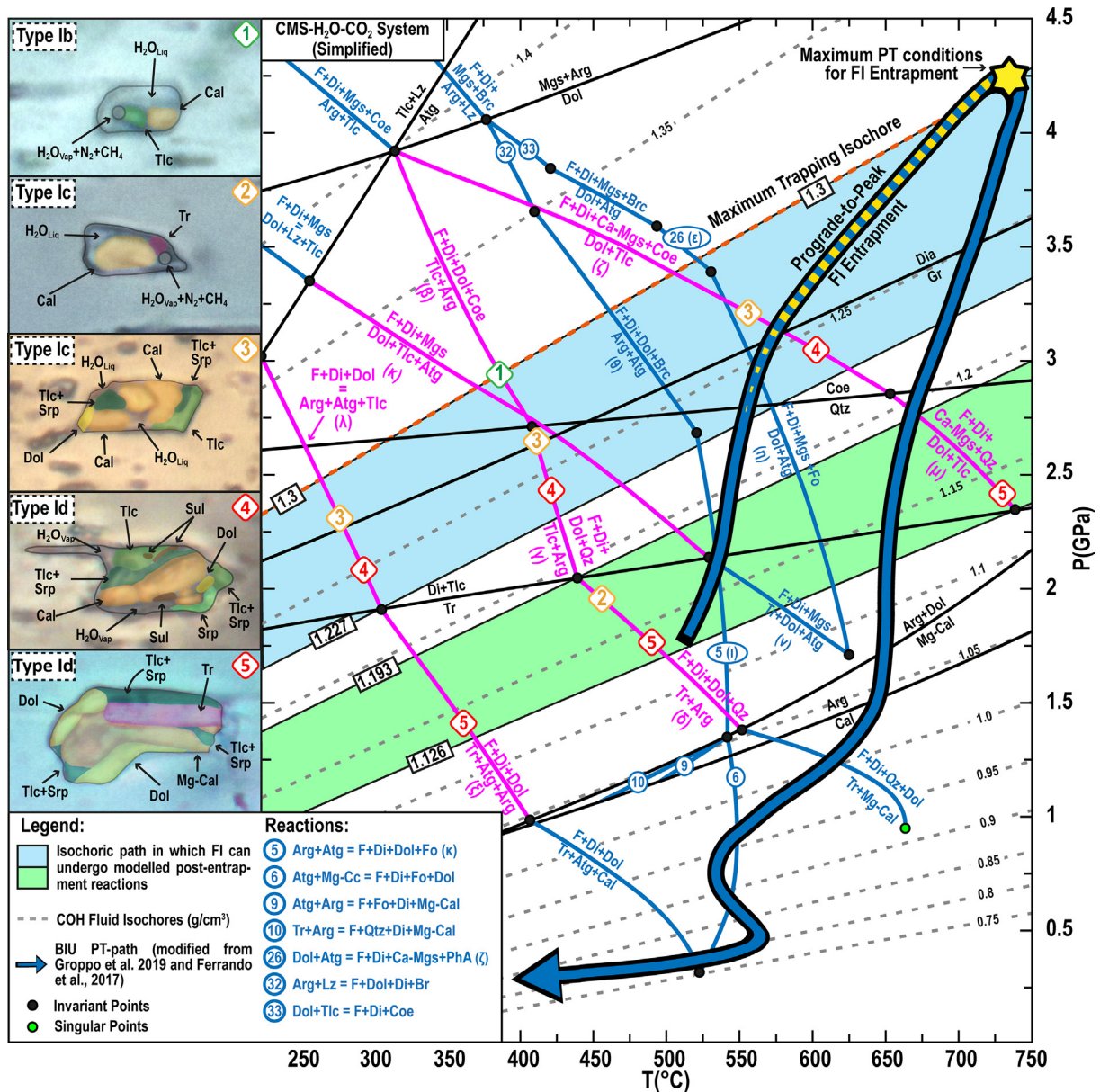


Fig. 8. Selected reactions from the general CMS-H₂O-CO₂ petrogenetic grid (Fig. 7) calculated to model post-entrapment reactions between host Di and the included fluid. Only reactions with the structure of reaction (α) are reported. Pink lines are the reactions selected for reproducing the observed mineral association within Early Type I fluid inclusions. Blue lines are reactions with the structure of reaction (α), which cannot reproduce the mineral association observed within Early Type I fluid inclusions. Black lines are all the other reactions that are relevant to understand the grid. The selected FI representative of the Early Type I FI re-equilibration stages are reported in the sketched photomicrographs on the left part of the figure. Correspondence between step-daughter minerals in the photomicrographs and the producing reactions is visualised with coloured numbers in diamonds. Dotted lines are isochores calculated for a COH fluid composed by H₂O = 99.95 mol%, CO₂ = 0.05 mol% (see text). The adopted EOS for fluid density calculation are Zhang and Duan (2005), for H₂O, and Sterner and Pitzer (1994) for CO₂. (For interpretation of the references to colour in this figure legend, the reader is referred to the web version of this article.)

fluid-host chemical interactions that the inclusions experienced during their isochoric exhumation paths.

Inclusion #1 (Type Ib) in Fig. 8 represents, among all the fluid inclusions, those still rich in fluid (Table 1) and with the simplest mineral association (calcite + talc; Table 1). This mineral association could have been produced by the isothermal reactions β and γ (Table 3). Reac-

tion β intersects the 1.3 g/cm³ maximum-trapping isochore at ~380 °C and ~2.95 GPa (Table 3; Fig. 8), defining an upper limit to the *P-T* conditions at which this reaction could have affected Type Ib fluid inclusions. Since these inclusions do not require a post-entrapment reaction located on a lower isochore than the 1.3 g/m³, we cannot rule out the possibility that included minerals in Type Ib

Table 2

Summary of the modelled peak mineral assemblage and co-existing CFMS-COHS electrolytic solute-bearing fluid (data extrapolated at the PT condition of the yellow star in [Supplementary Fig. 4](#)).

Peak Mineral Assemblage	Peak COHS Fluid composition		Peak COHS Fluid Structure				
	mol%	mol%	mol%	wt%			
Cpx	2.11	Si	0.04	CO ₂	0.05	0.11	Solvent
Ol	5.99	Mg	0.32	CH ₄	0.02	0.02	
Fluid	9.95	Fe	1.58·10 ⁻⁷	H ₂ S	0.02	0.04	Solutes
Arg	78.64	Ca	0.83	H ₂ O	96.30	88.50	
Dol	2.32	C	1.82	Ca-Si-Mg-Fe-S-C- bearing neutral and charged species	3.70	11.34	
Dia	0.08	H ₂	63.71				
Py	0.19	O ₂	33.13	Tot	100	100	
Chu	0.73	S ₂	0.14				
Tot	100	Tot	100				

FI (i.e., Tlc + Cal) can either be daughter or step-daughter minerals.

Inclusion #2 and #3 in [Fig. 8](#) belong to Type Ic fluid inclusions, i.e., fluid inclusions with an intermediate fluid/solid ratio. The observed mineral association is heterogeneous among the inclusions (see [Table 1](#)), and this can be explained with more than one evolutionary path ([Fig. 8](#)). Inclusion #2 is representative of the simplest Type Ic fluid inclusion ([Fig. 8](#)). The mineral association consists of large calcite and tremolite ([Table 1](#)). Although the large dimension of the calcite points to its incidental entrapment, at least part of the crystal could be overgrown during the reaction δ ([Table 3](#)). Inclusion #3 contains the most complex mineralogy (Cal + Tlc + Dol + Srp \pm Py; [Table 1](#)) and the lowest H₂O_{Liq} vol% observed in Type Ic fluid inclusions ([Fig. 8](#)). To reproduce the observed mineral association, multiple consecutive fluid-host reactions must be crossed along an isochoric path, possibly associated with incidental entrapment of CaCO₃. Calcite, talc, dolomite, and antigorite, requires that at least one, or more, of reactions β , γ , ϵ , ζ , η , θ , ι , κ and λ has been active. Among the hydrous silicates, antigorite is usually present in intergrowth aggregates with Tlc ([Fig. 5e](#)) but never associated with carbonates. So, the overall predominance of talc over antigorite supports the occurrence of Tlc-producing reactions, instead of reactions producing antigorite + carbonates only (ϵ , η , θ and ι). Among Tlc-producing reactions, reaction ζ is responsible for the presence of dolomite and reactions β or γ produced talc and aragonite (see Type Ib fluid inclusions). In addition, reactions λ and κ are considered responsible for the observed intergrowth of talc and antigorite. Notably, dolomite on the reactant side of reaction λ does not necessarily represent dissolved elements in the fluids. It could also represent a step-daughter mineral, previously produced by reaction ζ , that participates in a subsequent reaction.

Inclusions #4 and #5 in [Fig. 8](#) represent the multiphase-solid inclusions (Type Id fluid inclusions), i.e., those with the lowest vol% of fluid and the most complex mineral association ([Table 1](#)). Because inclusion #4 has the same mineral association as inclusion #3 (plus pyrite), it must have experienced the same post entrapment reactions $\zeta + \beta/\gamma + \kappa + \lambda$. However, the volume of the free fluid phase in inclusion #4 is lower than in #3. The presence of a prominent

offshoot suggests that inclusion #4 experienced further post-trapping modifications (see below). Inclusion #5 is filled only by crystals ([Fig. 8](#) and [Table 1](#)). The occurrence of tremolite, dolomite, talc, antigorite and calcite require that at least one, or more, of reactions μ , η , ν , ι , κ , δ and ξ has been active. Reactions η , ι and ν can be excluded for the same argument used above. Dolomite and talc are due to reactions μ and κ , with the latter also producing aragonite. Tremolite is due to reactions δ and ξ , which also produce further aragonite. Reaction θ is also responsible for the talc-antigorite intergrowths.

Regarding graphite and sulphides within Type Ic and Type Id FIs, their stability is unconstrained by this simplified chemical model. They are only rarely observed, but their presence could be overlooked because masked by the larger minerals. Thus, they could represent either incidentally trapped minerals or daughter minerals.

In conclusion, the CaCO₃ incidentally trapped or formed during fluid-host interactions in all Early Type I fluid inclusions was aragonite. Moreover, the solid inclusions of calcite and dolomite ([Fig. 3g](#)) are likely derived from accidental trapping within the growing Cpx II. The calcite now observed in the inclusions derives from the Arg-Cal transition, and Mg-calcite could also be formed at similar *P-T* conditions through reaction ϵ . The observed coexistence of all three serpentine minerals in the same mineral aggregates (i.e., Atg, Ctl and Lz) is explained by incomplete retrogression during the final stages of the rock exhumation history. Collectively, the reactions investigated here indicate that calcite/Mg-calcite (converted from aragonite), dolomite, talc, serpentine minerals and tremolite are step-daughter minerals. However, it is not possible to exclude that part of the trapped minerals is derived from direct precipitation from the trapped fluid (i.e. daughter minerals). This is especially true for those fluid inclusions whose composition still lies on the peak fluid-DM675 tie line ([Fig. 10](#); see below) and for Type Ib FI since there are no post-entrapment reactions that unambiguously constrain an isochore interval that does not include the maximum trapping isochore of 1.3 g/cm³: they could be considered unmodified FI. These fluid inclusions will fall within the upper part of the high fluid density light blue isochoric interval (i.e., they will follow a high-density isochoric decompressional path) in [Fig. 8](#). On the other hand, all the

Table 3

Table summarising all the reactions with the structure of reaction “ α ” that are considered capable to explain the mineral associations observed within Type I fluid inclusions. T and P values in brackets correspond to the T-P coordinates of the intersection between the maximum trapping isochore of 1.3 g/cm³ and that specific reaction. Reactions that affected Type I fluid inclusions (i.e., pink reactions in Fig. 8) are marked by bold “x”.

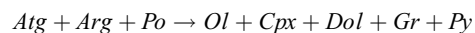
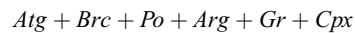
	Reactions		Lower to Upper Limits		Affected Fluid Inclusions			
	Host+H ₂ O + CO ₂	Dissolved cations	Step-Daughter minerals	T Range (°C)	P Range (GPa)	Ib	Ic	Id
β	Di + F	Dol + Coe (C, Mg, Si)	Arg + Tlc	~410–~310 (~380)	~2.8–~3.9 (~2.9)	X	X	
γ	Di + F	Dol + Qz (C, Mg, Si)	Arg + Tlc	~440–~410	~2.0–~2.8	X	X	
δ	Di + F	Dol + Qz (C, Mg, Si)	Arg + Tr	~440–~550	~2.0–~1.4			X
ϵ	Di + F	Ca-Mgs + PhA (C, Mg, Ca, Si)	Dol + Atg	~530–~490 (~520)	~3.4–~3.6 (~3.5)	X	X	
ζ	Di + F	Ca-Mgs + Coe (C, Mg, Ca, Si)	Dol + Tlc	~650–~310 (~505)	~2.8–~3.9 (~3.4)	X	X	
η	Di + F	Mgs + Fo (C, Mg, Si)	Dol + Atg	~625–~530	~1.7–~3.4	X	X	
θ	Di + F	Dol + Brc (C, Mg, Ca, Si)	Arg + Atg	~520–~410 (~460)	~2.7–~3.7 (~3.2)	X	X	
ι	Di + F	Fo + Dol (C, Mg, Ca, Si)	Arg + Atg	~540–~520	~1.3–~2.7	X	X	
κ	Di + F	Mgs (C, Mg)	Dol + Tlc + Atg	~530–~260 (~375)	~2.2–~3.3 (~2.8)	X	X	
λ	Di + F	Dol (C, Mg, Ca)	Arg + Tlc + Atg	~300–~225 (~260)	~1.9–~3 (~2.5)		X	
μ	Di + F	Ca-Mgs + Qz (C, Mg, Ca, Si)	Dol + Tlc	~740–~650	~2.3–~2.8		X	
ν	Di + F	Mgs (C, Mg)	Tr + Dol + Atg	~625–~530	~1.7–~2.2		X	
ξ	Di + F	Dol (C, Mg, Ca)	Tr + Atg + Arg	~400–~300	~1–~1.9		X	

Type Ic and Id FI that record some chemical interaction with the host clinopyroxene, without Tr-production, should have reached the LT part of the high-density isochoric interval (light blue field in Fig. 8). On the contrary, Type Ic and Id fluid inclusions that contain Tr require post-entrapment reactions located at lower pressure: these fluid inclusions followed the lower density isochoric decompressional path (green field in Fig. 8).

6.2. HP-UHP rock-fluid evolution predicted by electrolytic-fluid thermodynamics

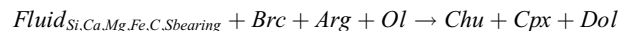
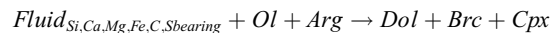
The modelled prograde metamorphic evolution of both rock and associated fluid is summarised below (Fig. 9; Supplementary Fig. 4).

At HP conditions (1.8–2.95 GPa), most of the fluid is released by the discontinuous (Brc-out) and continuous (Atg-out; see continuously decreasing Atg abundance in Fig. 9b) dehydration reactions (Fig. 9; mineral abbreviation after Whitney and Evans, 2010):

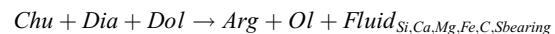


The fluid is predicted to be an aqueous fluid with > 99 mol% of H₂O and with minor amounts of both volatile molecular species (CO₂, CH₄ and H₂S; Fig. 9d) and non-volatile solutes (molality < 0.38 mol/kg and < 1 mol%; Fig. 9c, d) originated by partial dissolution of the mineral assemblage. At this stage, the Cpx is likely produced as the Cpx II (Ferrando et al., 2017) that traps the coexisting fluid, carbonates and graphite (Fig. 3c, e, g).

At UHP conditions (>2.95 GPa), the amount of fluid present in the system is nearly constant and only marginally affected by the two continuous hydration reactions (Brc-in and Brc → Chu, respectively, in Fig. 9):



These reactions, as well the change (i.e., increase) in the P-T gradient, boost the whole-rock dissolution processes, as recorded by the constant increase in the concentrations of non-volatile solute species and fluid molality (Fig. 9c-d and Table 2) up to the metamorphic peak (4.3 GPa and 730 °C) from 1 mol% to 3.61 mol% and from 0.5 mol/kg to 2.0 mol/kg. The peak fluid has been sampled by Early Type I FI trapped in Cpx III. This Cpx generation continues to precipitate up to the point at which the P-T path crosses the dehydration reaction Chu-out (Fig. 9):



This reaction is responsible for the last event of fluid release and of rock dissolution (Fig. 9a, b), which bumps the rock dissolution, especially of carbonates (marked by a slight jump in the content of C and Ca in the fluid, Fig. 9c), increasing the fluid molality to nearly 2.1 mol/kg (Fig. 9d).

6.3. Nature of the peak metamorphic fluid

Based on the assumption of a binary H₂O–CO₂ fluid model, previous studies on the Costa Monforte marble lens demonstrated the stability of a CO₂-poor aqueous fluid at UHP conditions (Castelli et al., 2007; Ferrando et al., 2017). Limiting the discussion to dolomitic marbles, Castelli et al. (2007) calculated that a CO₂-poor aqueous fluid with CO₂ < 0.12 mol% was stable in a CMAS–H₂O–CO₂ rock system (Fig. 10a, b). More recently, analysis of sample DM675 (i.e., the same sample studied in this work) constrained the CO₂ content of the UHP fluid in the range 0.03–0.08 mol% (Ferrando et al., 2017; Fig. 10a, b). In the present work, molecular volatiles other than H₂O (i.e., CO₂ + CH₄ + H₂S) comprise up to 0.09 mol% of the fluid. If CO₂ and H₂O of the electrolytic fluid modelled in this work are normalised to 100 mol%, the resulting composition is an aqueous fluid with CO₂ = 0.052 mol%, which is perfectly in agreement with the estimates of Castelli et al. (2007) and Ferrando et al. (2017) (Fig. 10b).

The peak electrolytic fluid modelled by thermodynamics for the sample DM675 is a solute-bearing aqueous fluid with 11.34 wt% of solutes, ~0.17 wt% of CO₂ + CH₄ + H₂S, and 88.50 wt% of H₂O (Table 2). This solute concentration is appropriate for brine-like fluids since they are characterised by < 30 wt% of solute content (Frezza and Ferrando, 2015). Regarding the presence of dissolved chlorides, their occurrence is testified by: i) microthermometric measurements, ii) the presence of Cl-bearing precipitates in opened fluid inclusions (Fig. 6) and iii) the shape of the Raman bands of H₂O_{Liq} (Fig. 5h). However, when mass balanced, a salinity from 9.6 to 18.7 wt% of the residual fluid indicates very low Cl content, especially if compared to other ions (e.g., S₂, Table 1; see below). Thus, we assume that, in Early Type I fluid inclusions, the Cl-content is so low that it is thermodynamically irrelevant. Interestingly, the modelled solute-bearing aqueous COHS fluid can transport an appreciable solute content (11.34 wt% at the UHP peak) without any Cl helping its solubilisation.

6.4. Validity of modified fluid inclusions as micro-samples of HP–UHP fluids

The modelling of the fluid–host reactions (Fig. 8) suggests that Type Ib fluid inclusions experienced no (or limited) chemical interactions between the host clinopyroxene and the trapped fluid. On the contrary, Type Ic and Id fluid inclusions strongly interacted with the host clinopyroxene. To test if other typologies of post-entrapment modifications occurred in the fluid inclusions and their role in the preservation of the former chemical composition of the fluid, we compared the peak fluid composition calculated with an electrolytic-fluid model (Table 2; Fig. 9c, d) with the fluid inclusion bulk compositions reconstructed from each analysed Type I fluid inclusion (Table 1).

In a closed system, such as that of the Costa Monforte marble lens (Castelli et al. 2007; Ferrando et al., 2017), the ratio between the main rock-forming elements (i.e., Si, Mg, Fe, Ca, C, S) and the coexisting fluid is constant and given by the dissolution of bulk composition of the dissolv-

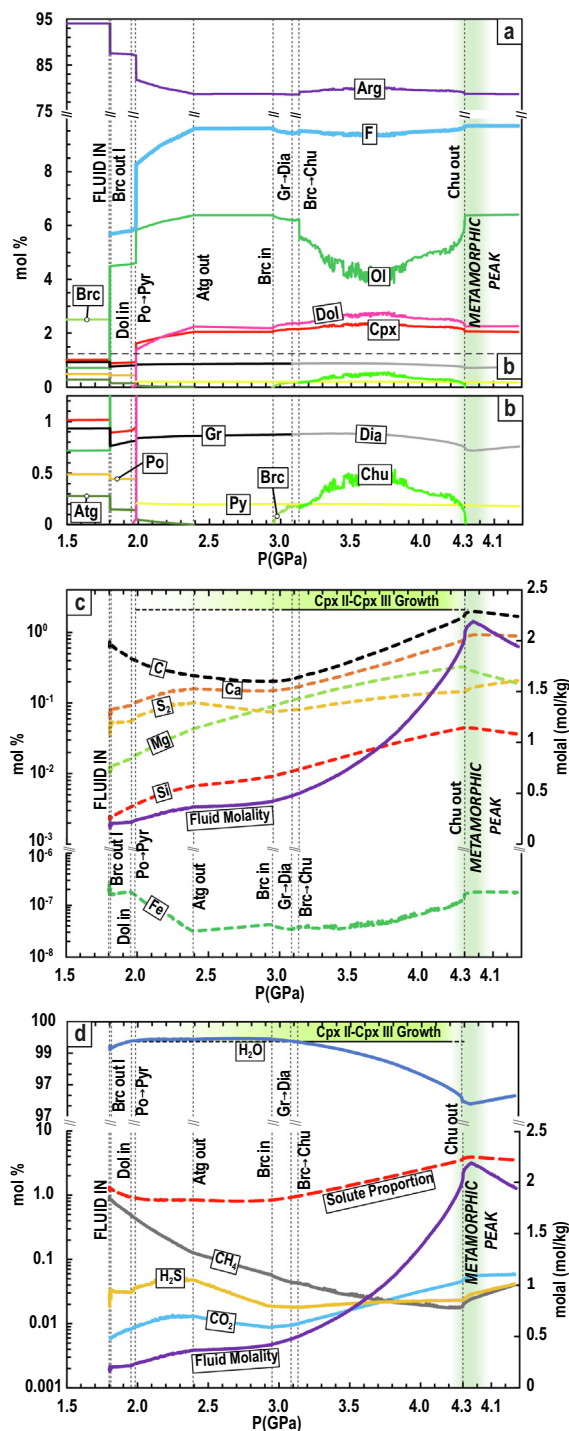


Fig. 9. Mineral and fluid evolution of sample DM675 during prograde-to-peak BIU P–T path (yellow dashed line in Fig. 1b; source: isochemical phase diagram in Supplementary Fig. 4). (a, b) Molar variations of mineral and fluid phases along the studied P–T path. (c) Molar variations of the elements in the prograde-to-peak fluid generated by progressive mineral dissolution of the rock-forming minerals. (d) Molar evolution of the solvent species (H₂O, CO₂, CH₄, H₂S) and of the solute content in the fluid during the rock HP–UHP evolution. In both (c) and (d), the evolution of the fluid molality is also reported. (For interpretation of the references to colour in this figure legend, the reader is referred to the web version of this article.)

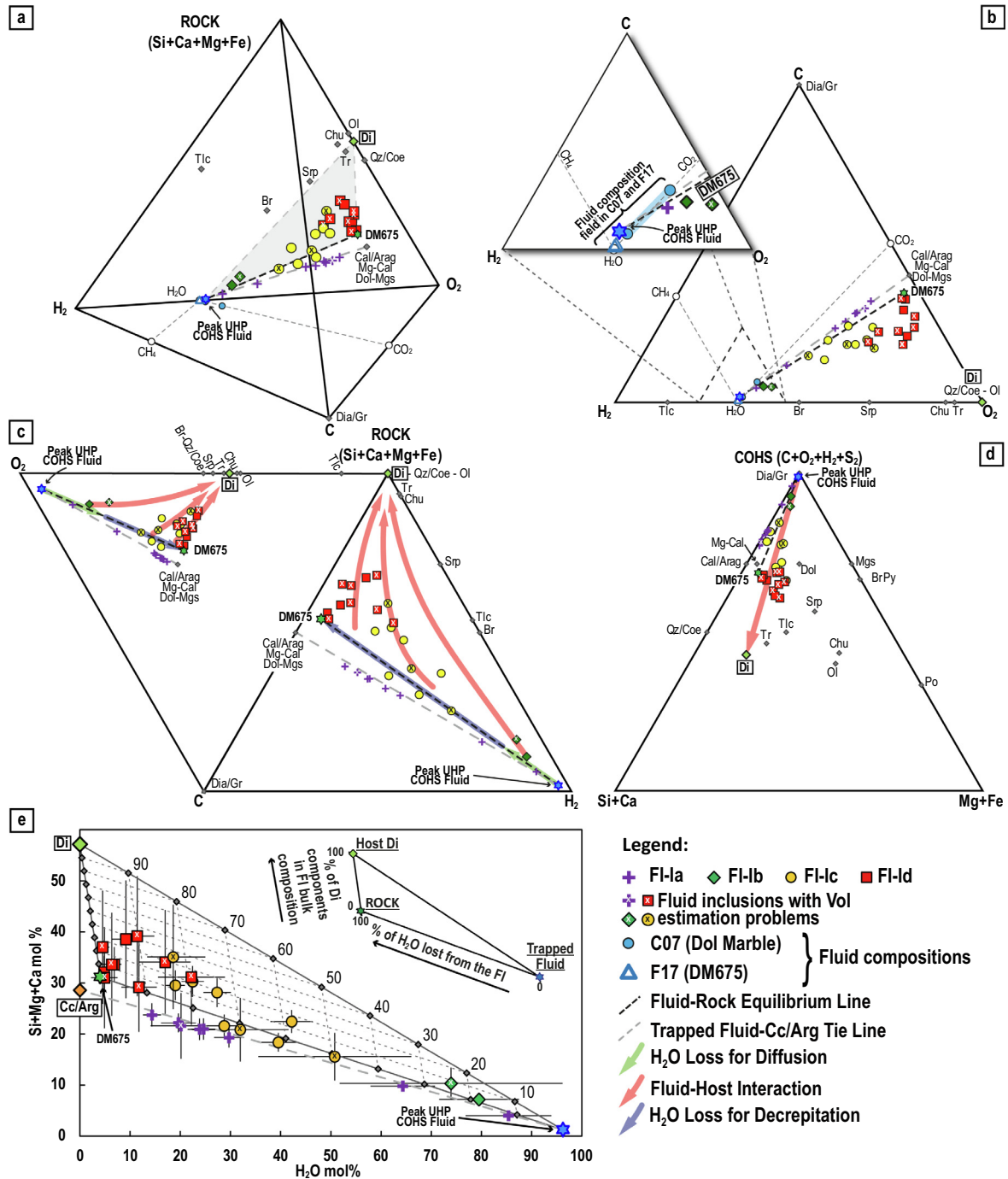


Fig. 10. (a) Tetrahedron describing the chemical relationships between reconstructed fluid inclusion compositions, modelled peak fluid, bulk-rock, and mineral phases characterising the studied system. The grey triangle represents the plane whose vertices are the modelled fluid, the bulk rock, and the host Di; because this plane contains the measured fluid inclusion compositions, it allows recognising the different types and extents of post-trapping modifications. (b-c) Ternary plots obtained from the tetrahedron in (a). (b) C-O₂-H₂ face of (a): the inset shows the comparison between the modelled peak fluid composition and the fluid compositions in the Costa Monforte marble lens calculated by previous works (i.e., [Castelli et al., 2007](#): C07; [Ferrando et al., 2017](#): F17). (c) Double ternary plot of H₂ and O₂ against the other rock-forming cations and C, showing a coupled depletion trend (compared to the peak modelled fluid) of both H₂ and O₂, suggesting H₂O loss from the inclusions. Deviation from the peak fluid-rock tie-line reflects the influence of the host or included minerals on the fluid inclusion bulk composition. (d) Ternary plot where silicates and carbonates are differentiated to better evaluate the mineral contributions to the fluid inclusion bulk composition, especially the host Di, and Tlc and Srp (since they have strong volumetric estimation errors). (e) Discrimination diagram showing the measured FI composition, and relative estimation error, in terms of molar H₂O and Si + Ca + Mg, to highlight the relationships between the fluid inclusion modified composition and the host Di, the original COHS peak fluid composition and the bulk-rock composition (DM675). This triangle highlights the amount of Di contamination within fluid inclusions and the degree of H₂O loss from the same fluid inclusions.

(ex-aragonite) crystal. Fig. 10e also reveals that Type Ib fluid inclusions have experienced only 2–8 mol % of host Di contamination (Table 4). This is in line with the small dimensions of the step-daughter talc and the preservation of most of the aqueous fluid (76–82 mol%; Table 4).

On the other hand, in Type Ic fluid inclusions, a relevant Di contamination is paired with a considerable H₂O loss (up to 35 mol% of Di component; from 17 to 51 mol% of the original H₂O content is still present; Table 4). As expected, Type Id fluid inclusions are characterised by the lowest amount of preserved H₂O (from 0 to 21 mol%), and by the highest Di component contamination (from 2 to 42 mol%; Table 4). The relevant addition of diopside component (i.e., Ca + Mg + Si) from the host clinopyroxene allowed the growth of talc, serpentine minerals, and if the fluid loss was enough to drastically reduce the fluid density (i.e., moving the inclusion to a lower density isochore: from the light blue isochoric field to the light green one in Fig. 8), tremolite. In addition to silicates, dolomite and aragonite would also form (and probably precipitate as H₂O is lost from the inclusion). Interestingly, some multiphase-solid inclusions (Type Id fluid inclusions) record only a minimal Di contamination (from 0 to 5 mol% of Di component), but a nearly complete H₂O loss (residual H₂O component ranging from 1 to 8 mol%).

Finally, Fig. 10 shows that even the rare Type Ib fluid inclusions that could have been regarded as unmodified by fluid-host reactions record water loss. This process is recognisable only from the solute concentrations predicted by the electrolytic-fluid model. At the opposite extreme, fluid inclusions that are entirely filled by solids (i.e., Type Id multiphase-solid inclusions) preserve the elemental ratios of the originally trapped UHP fluid since they lost mainly H₂O and only marginally reacted with the host Di. Thus, no fluid inclusion seems completely unmodified: all fluid inclusions record a sum of post-entrapment H₂O loss and chemical interaction with the host mineral. However, not all fluid inclusions lost their chemical validity because those that experienced only H₂O loss, regardless of the amounts of minerals included in them, may still bear reliable chemical information.

The geologic significance of the collinearity between reconstructed fluid inclusion composition and the thermodynamically modelled peak fluid composition confirms the closed system behaviour of the studied marble lens during active subduction, as reported by previous works on Costa Monforte marble lens (Castelli et al., 2007; Ferrando et al., 2017).

7. CONCLUSIONS

HP-UHP fluid inclusions give chemical and physical information about deep metamorphic fluids. They are known to be highly prone to modifications during rock exhumation. The present multidisciplinary work shows how even apparently highly modified FIs can preserve the chemical composition of the formerly trapped HP-UHP fluid.

In this study, we also demonstrate how, in carbonate systems, the progressive re-equilibration of fluid inclusions due to a combination of H₂O diffusion and fluid loss and host-fluid chemical interactions can transform an aqueous fluid inclusion in a multiphase-solid inclusion (with up to 42 mol% of Di contamination and between 18 mol% to 99 mol% of the original H₂O lost). This study also confirms that the fluid inclusions least affected by post-trapping modifications are those characterised by small dimensions, negative crystal shape, the highest volume of preserved fluid, and the lowest volume of crystals. This confirms how large fluid inclusions with irregular shapes, the presence of crystal lattice defects, the chemical propension of minerals characterised by solid solutions to chemically interact with trapped fluid are all factors favouring post-entrapment modifications (Bodnar, 2003). In addition, fluid inclusions trapped in deep rocks (both metamorphic rocks equilibrated at HP and UHP conditions and mantle rocks) also experienced extreme changes in P and T, from their equilibration conditions to those on the surface, that further promote post-entrapment re-equilibration processes (Andersen et al., 1984; Heinrich and Gottschalk, 1995; Frezzotti et al., 2012a; Frezzotti and Ferrando, 2015; Carvalho et al., 2020). The identification of chemically preserved fluid inclusions is fundamental for further analysis on the chemistry of UHP fluids (e.g., trace element content). In turn, the thermodynamic modelling of electrolytic fluids helps to identify the degree of cryptic and non-cryptic post-entrapment modifications experienced by each HP-UHP fluid inclusion.

Conventional wisdom indicates that subducted carbonate sediment layers do not encounter relevant decarbonation reactions (thus not considering carbonate dissolution) at sub-arc conditions, releasing little or no CO₂. In Costa Monforte marble lens, C mobilised as molecular CO₂ (i.e., modelled as derived from decarbonation reactions) reaches up to 0.03 mol% in a classical H₂O-CO₂ mixture. On the other hand, C mobilised by carbonate dissolution in aqueous fluid, whether internally or externally derived (e.g., Frezzotti et al., 2011; Connolly and Galvez, 2018; Frezzotti, 2019; Menzel et al., 2020; van Schroyen Lantman et al., 2021; Farsang et al., 2021) and speciated as ionic ligands (i.e., HCO₃⁻, CO₃²⁻), organic functional groups (i.e., CHOO⁻; CH₃COO⁻), neutral carboxylic acids and hydrocarbons, represents 1.8 mol% of the total solute-bearing fluid. Although a small absolute value, it is roughly two orders of magnitude higher than C mobilised as molecular CO₂. Thus, the capability of the electrolytic modelling to reproduce a UHP fluid composition, that is in line with what is observed within natural UHP fluid inclusions in the simple CFMS-COHS chemical system, is promising for further investigations in more complex chemical systems.

Declaration of Competing Interest

The authors declare that they have no known competing financial interests or personal relationships that could have appeared to influence the work reported in this paper.

ACKNOWLEDGEMENTS

This paper is a part of A.M.'s Ph.D. thesis, and electrolytic fluid modelling was performed as a visiting student at ETH (Zurich). We thank three anonymous reviewers for their comments and suggestions that significantly clarified and greatly improved an earlier version of this manuscript. The authors also thank the Editor in Chief Jeffrey Catalano and the Associate Editor Weidong Sun for the editorial handling of this manuscript. We acknowledge L. Martire, for the assistance during cathodoluminescence analyses, and R. Cosio, for assistance during the acquisition of whole section X-ray maps. Laboratory work was funded by the Italian Ministry of University and Research (PRIN 2017, Project n°: 2017LMNLAW), and by the FERSMASCON by the University of Torino to S.F.; Raman facilities were provided by the Interdepartmental Center "G. Scansetti" for studies on asbestos and other toxic particulates at the University of Torino.

APPENDIX A. SUPPLEMENTARY MATERIAL

Supplementary data to this article can be found online at <https://doi.org/10.1016/j.gca.2021.08.044>.

REFERENCES

- Ague J. J. and Nicolescu S. (2014) Carbon dioxide released from subduction zones by fluid-mediated reactions. *Nat. Geos.* **7**(5), 355–360.
- Andersen T., O'Reilly S. Y. and Griffin W. L. (1984) The trapped fluid phase in upper mantle xenoliths from Victoria, Australia: implications for mantle metasomatism. *Contrib. Mineral. Petr.* **88**(1–2), 72–85.
- Anovitz L. M. and Essene E. J. (1987) Phase equilibria in the system $\text{CaCO}_3\text{-MgCO}_3\text{-FeCO}_3$. *J. Petrol.* **28**(2), 389–415.
- Bakker R. J. (2009) Re-equilibration of fluid inclusions: Bulk-diffusion. *Lithos* **112**(3–4), 277–288.
- Bakker R. J. and Jansen J. B. H. (1991) Experimental post-entrapment water loss from synthetic $\text{CO}_2\text{-H}_2\text{O}$ inclusions in natural quartz. *Geochim. Cosmochim. Acta* **55**(8), 2215–2230.
- Bakker R. J. and Jansen J. B. H. (1990) Preferential water leakage from fluid inclusions by means of mobile dislocations. *Nature* **345**(6270), 58–60.
- Bebout G. E. (2013) Metasomatism in subduction zones of subducted oceanic slabs, mantle wedges, and the slab-mantle interface. In *Metasomatism and the chemical transformation of rock* (eds. D. Harlov and H. Austrheim). Springer, Berlin, Heidelberg, pp. 289–349.
- Bekaert D. V., Turner S. J., Broadley M. W., Barnes J. D., Halldórsson S. A., Labidi J., Wade J., Walowski K. J. and Barry P. H. (2020) Subduction-driven volatile recycling: A global mass balance. *Annu. Rev. Earth Pl. Sc.* **49**, 37–70.
- Burke E. A. (2001) Raman microspectrometry of fluid inclusions. *Lithos* **55**(1–4), 139–158.
- Carvalho B. B., Bartoli O., Cesare B., Tacchetto T., Gianola O., Ferri F., Aradi L. and Szabó C. (2020) Primary CO_2 -bearing fluid inclusions in granulitic garnet usually do not survive. *Earth. Plan. Sci.* **536** 116170.
- Castelli D., Compagnoni R., Lombardo B., Angiboust S., Balestro G., Ferrando S., Groppo C., Hirajima T. and Rolfo F. (2014) Crust-mantle interactions during subduction of oceanic & continental crust. *10th International Eclogitise Conference, Courmayeur (Aosta, Italy)-Post-conference excursions: September 9-10, 2013*.
- Castelli D., Rolfo F., Groppo C. and Compagnoni R. (2007) Impure marbles from the UHP Brossasco-Isasca Unit (Dora-Maira Massif, western Alps): evidence for Alpine equilibration in the diamond stability field and evaluation of the X (CO_2) fluid evolution. *J. Metamorph. Geol.* **25**(6), 587–603.
- Chopin C. (1984) Coesite and pure pyrope in high-grade blueschists of the Western Alps: a first record and some consequences. *Contrib. Mineral. Petr.* **86**(2), 107–118.
- Clift P. D. (2017) A revised budget for Cenozoic sedimentary carbon subduction. *Rev. Geophys.* **55**(1), 97–125.
- Compagnoni R. and Rolfo F. (2003) UHPM units in the Western Alps. In *Ultrahigh pressure metamorphism, EMU Notes in Mineralogy*, 5 (eds. D. A. Carwell and R. Compagnoni). Eötvös University Press, Budapest, pp. 13–49.
- Compagnoni R., Hirajima T. and Chopin C. (1995) Ultra-high-pressure metamorphic rocks in the Western Alps. In *Ultrahigh Pressure Metamorphism* (eds. R. G. Coleman and X. Wang). Cambridge University Press, Cambridge, pp. 206–243.
- Connolly J. A. D. (1990) Multivariable phase diagrams; an algorithm based on generalised thermodynamics. *Am. J. Sci.* **290**(6), 666–718.
- Connolly J. A. and Galvez M. E. (2018) Electrolytic fluid speciation by Gibbs energy minimisation and implications for subduction zone mass transfer. *Earth Planet. Sc. Lett.* **501**, 90–102.
- Connolly J. A. and Trommsdorff V. (1991) Petrogenetic grids for metacarbonate rocks: pressure-temperature phase-diagram projection for mixed-volatile systems. *Contrib. Mineral. Petr.* **108** (1–2), 93–105.
- De Santis R., Breedveld G. J. F. and Prausnitz J. M. (1974) Thermodynamic properties of aqueous gas mixtures at advanced pressures. *Ind. Eng. Chem. Proc. Dd.* **13**(4), 374–377.
- Deer W., Howie R. A. and Zussman J. (2013) *An introduction to the rock-forming minerals*. The Mineralogical Society London, p. p. 498.
- Di Vincenzo G., Tonarini S., Lombardo B., Castelli D. and Ottolin L. (2006) Comparison of $^{40}\text{Ar}\text{-}^{39}\text{Ar}$ and Rb-Sr data on phengites from the UHP Brossasco-Isasca Unit (Dora Maira Massif, Italy): implications for dating white mica. *J. Petrol.* **47** (7), 1439–1465.
- Evans K. A., Powell R. and Holland T. J. B. (2010) Internally consistent data for sulphur-bearing phases and application to the construction of pseudosections for mafic greenschist facies rocks in $\text{Na}_2\text{O-CaO-K}_2\text{O-FeO-MgO-Al}_2\text{O}_3\text{-SiO}_2\text{-CO}_2\text{-O-S-H}_2\text{O}$. *J. Metamorph. Geol.* **28**(6), 667–687.
- Farsang S., Louvel M., Zhao C., Mezouar M., Rosa A. D., Widmer R. N., Feng X. and Redfern S. A. (2021) Deep carbon cycle constrained by carbonate solubility. *Nat. Comm.* **12**(1), 1–9.
- Ferrando S., Frezzotti M. L., Petrelli M. and Compagnoni R. (2009) Metasomatism of continental crust during subduction: the UHP whiteschists from the Southern Dora-Maira Massif (Italian Western Alps). *J. Metamorph. Geol.* **27**(9), 739–756.
- Ferrando S., Groppo C., Frezzotti M. L., Castelli D. and Proyer A. (2017) Dissolving dolomite in a stable UHP mineral assemblage: Evidence from Cal-Dol marbles of the Dora-Maira Massif (Italian Western Alps). *Am. Mineral.* **102**(1), 42–60.
- Ferrando S., Petrelli M. and Frezzotti M. L. (2019) Gradual and selective trace-element enrichment in slab-released fluids at subarc depths. *Sci. Rep.-Uk* **9**(1), 1–9.
- Frezzotti M. L. (2019) Diamond growth from organic compounds in hydrous fluids deep within the Earth. *Nat. Commun.* **10**(1), 1–8.
- Frezzotti M. L. and Ferrando S. (2015) The chemical behavior of fluids released during deep subduction based on fluid inclusions. *Am. Mineral.* **100**(2–3), 352–377.

- Frezzotti M. L., Ferrando S., Tecce F. and Castelli D. (2012a) Water content and nature of solutes in shallow-mantle fluids from fluid inclusions. *Earth Planet. Sc. Lett.* **351**, 70–83.
- Frezzotti M. L., Tecce F. and Casagli A. (2012b) Raman spectroscopy for fluid inclusion analysis. *J. Geochem. Explor.* **112**, 1–20.
- Frezzotti M. L., Selverstone J., Sharp Z. D. and Compagnoni R. (2011) Carbonate dissolution during subduction revealed by diamond-bearing rocks from the Alps. *Nat. Geosci.* **4**(10), 703–706.
- Galvez M. E., Connolly J. A. and Manning C. E. (2016) Implications for metal and volatile cycles from the pH of subduction zone fluids. *Nature* **539**, 420–424.
- Galvez M. E., Manning C. E., Connolly J. A. and Rumble D. (2015) The solubility of rocks in metamorphic fluids: A model for rock-dominated conditions to upper mantle pressure and temperature. *Earth Planet. Sci. Lett.* **430**, 486–498.
- Gauthiez-Putallaz L., Rubatto D. and Hermann J. (2016) Dating prograde fluid pulses during subduction by in situ U-Pb and oxygen isotope analysis. *Contrib. Mineral. Petr.* **171**(2), 15.
- Gebauer D. H. P. S., Schertl H. P., Brix M. and Schreyer W. (1997) 35 Ma old ultrahigh-pressure metamorphism and evidence for very rapid exhumation in the Dora Maira Massif, Western Alps. *Lithos* **41**(1–3), 5–24.
- Groppo C., Ferrando S., Gilio M., Botta S., Nosenzo F., Balestro G., Festa A. and Rolfo F. (2019) What's in the sandwich? New P-T constraints for the (U)HP nappe stack of southern Dora-Maira Massif (Western Alps). *Eur. J. Mineral.* **31**(4), 665–683.
- Guild M. and Shock E. L. (2020) Predicted Speciation of Carbon in Subduction Zone Fluids. In *Carbon in Earth's Interior, Geophysical Monograph 249* (eds. Craig E. Manning, Jung-F Lin and Wendy L. Mao). American Geophysical Union and John Wiley and Sons, Inc., pp. 285–302.
- Hall D. L. and Bodnar R. J. (1990) Methane in fluid inclusions from granulites: a product of hydrogen diffusion? *Geochim. Cosmochim. Acta* **54**, 641–651.
- Hall D. L. and Sterner S. M. (1993) Preferential water loss from synthetic fluid inclusions. *Contrib. Mineral. Petr.* **114**(4), 489–500.
- Hall D. L., Bodnar R. J. and Craig J. R. (1991) Evidence for postentrapment diffusion of hydrogen into peak metamorphic fluid inclusions from the massive sulfide deposit at Ducktown, Tennessee. *Am. Mineral.* **76**, 1344–1355.
- Heinrich W. and Gottschalk M. (1995) Metamorphic reactions between fluid inclusions and mineral hosts. I. Progress of the reaction calcite + quartz = wollastonite + CO₂ in natural wollastonite-hosted fluid inclusions. *Contrib. Mineral. Petr.* **122** (1–2), 51–61.
- Helgeson H. C. and Kirkham D. H. (1974a) Theoretical prediction of the thermodynamic behavior of aqueous electrolytes at high pressures and temperatures; I, Summary of the thermodynamic/electrostatic properties of the solvent. *Am. J. Sci.* **274** (10), 1089–1198.
- Helgeson H. C. and Kirkham D. H. (1974b) Theoretical prediction of the thermodynamic behavior of aqueous electrolytes at high pressures and temperatures; II, Debye-Huckel parameters for activity coefficients and relative partial molal properties. *Am. J. Sci.* **274**(10), 1199–1261.
- Helgeson H. C. and Kirkham D. H. (1976) Theoretical prediction of thermodynamic properties of aqueous electrolytes at high pressures and temperatures. III. Equation of state for aqueous species at infinite dilution. *Am. J. Sci.* **276**(2).
- Helgeson H. C., Kirkham D. H. and Flowers G. C. (1981) Theoretical prediction of the thermodynamic behavior of aqueous electrolytes by high pressures and temperatures; IV, Calculation of activity coefficients, osmotic coefficients, and apparent molal and standard and relative partial molal properties to 600 degrees C and 5kb. *Am. J. Sci.* **281**(10), 1249–1516.
- Holland T. and Powell R. (1991) A compensated-Redlich-Kwong (CORK) equation for volumes and fugacities of CO₂ and H₂O in the range 1 bar to 50 kbar and 100–1600 C. *Contrib. Mineral. Petr.* **109**(2), 265–273.
- Holland T. J. B. and Powell R. (2011) An improved and extended internally consistent thermodynamic dataset for phases of petrological interest, involving a new equation of state for solids. *J. Metamorph. Geol.* **29**(3), 333–383.
- Huang F. and Sverjensky D. A. (2019) Extended Deep Earth Water Model for predicting major element mantle metasomatism. *Geochim. Cosmochim. Acta* **254**, 192–230.
- Huang F., Daniel I., Cardon H., Montagnac G. and Sverjensky D. A. (2017) Immiscible hydrocarbon fluids in the deep carbon cycle. *Nat. Commun.* **8**(1), 1–8.
- Huizenga J. M. (2001) Thermodynamic modelling of C–O–H fluids. *Lithos* **55**(1–4), 101–114.
- Karlsen K. S., Conrad C. P. and Magni V. (2019) Deep water cycling and sea level change since the breakup of Pangea. *Geochem. Geophys. Geosy.* **20**(6), 2919–2935.
- Kawamoto T., Hertwig A., Schertl H. P. and Maresch W. V. (2018) Fluid inclusions in jadeite and jadeite-rich rock from serpentinite mélanges in northern Hispaniola: Trapped ambient fluids in a cold subduction channel. *Lithos* **308**, 227–241.
- Kelemen P. B. and Manning C. E. (2015) Reevaluating carbon fluxes in subduction zones, what goes down, mostly comes up. *P. Natl. Acad. Sci. USA* **112**(30), E3997–E4006.
- Li Y. (2017) Immiscible CHO fluids formed at subduction zone conditions. *Geochem. Perspect. Lett* **3**, 12–21.
- Li J. L., Schwarzenbach E. M., John T., Ague J. J., Huang F., Gao J., Klemd R., Whitehouse M. J. and Wang X. S. (2020a) Uncovering and quantifying the subduction zone sulfur cycle from the slab perspective. *Nat. Commun.* **11**(1), 1–12.
- Li C. Y., Sun S. J., Guo X. and Zhu H. L. (2020b) Recent progresses in plate subduction and element recycling. *Solid Earth* **5**(1), 1–7.
- Macris C. A., Newton R. C., Wykes J., Pan R. and Manning C. E. (2020) Diopside, enstatite and forsterite solubilities in H₂O and H₂O-NaCl solutions at lower crustal and upper mantle conditions. *Geochim. Cosmochim. Acta* **279**, 119–142.
- Manning C. E. (2004) The chemistry of subduction-zone fluids. *Earth Planet. Sc. Lett.* **223**(1–2), 1–16.
- Manning C. E. and Frezzotti M. L. (2020) Fluids in Subduction Zones and the Upper Mantle. *Elements* **16**(6), 395–400.
- Mavrogenes J. A. and Bodnar R. J. (1994) Hydrogen movement into and out of fluid inclusions in quartz: experimental evidence and geologic implications. *Geochim. Cosmochim. Acta* **58**(1), 141–148.
- Menzel M. D., Garrido C. J. and Sánchez-Vizcaíno V. L. (2020) Fluid-mediated carbon release from serpentinite-hosted carbonates during dehydration of antigorite-serpentinite in subduction zones. *Earth. Plan. Sci.* **531** 115964.
- Morgan G. B., I-Ming C., Pateris C. and Olsen S. N. (1993) Re-equilibration of CO₂ fluid inclusions at controlled hydrogen fugacities. *J. Metamorph. Geol.* **11**, 155–164.
- Mysen B. (2019) Nitrogen in the Earth: abundance and transport. *Proceed. Earth. Plan. Sci.* **6**(1), 1–15.
- Oakes C. S., Bodnar R. J. and Simonson J. M. (1990) The system NaCl-CaCl₂-H₂O: I. The ice liquidus at 1 atm total pressure. *Geochim. Cosmochim. Acta* **54**(3), 603–610.
- Ortolano G., Visalli R., Godard G. and Cirrincione R. (2018) Quantitative X-ray Map Analyser (Q-XRMA): A new GIS-based statistical approach to Mineral Image Analysis. *Comput. Geosci.* **115**, 56–65.

- Padrón-Navarta J. A., Sánchez-Vizcaíno V. L., Hermann J., Connolly J. A., Garrido C. J., Gómez-Pugnaire M. T. and Marchesi C. (2013) Tschermak's substitution in antigorite and consequences for phase relations and water liberation in high-grade serpentinites. *Lithos* **178**, 186–196.
- Peccerillo A. and Frezzotti M. L. (2015) Magmatism, mantle evolution and geodynamics at the converging plate margins of Italy. *J. Geol. Soc. London* **172**(4), 407–427.
- Peng W., Zhang L., Menzel M. D., Vitale Brovarone A., Tumiati S., Shen T. and Hu H. (2020) Multistage CO₂ sequestration in the subduction zone: Insights from exhumed carbonated serpentinites, SW Tianshan UHP belt, China. *Geochim. Cosmochim. Acta* **270**, 218–243.
- Petriglieri J. R., Salvioli-Mariani E., Mantovani L., Tribaudino M., Lottici P. P., Laporte-Magoni C. and Bersani D. (2015) Micro-Raman mapping of the polymorphs of serpentine. *J. Raman. Spectrosc.* **46**(10), 953–958.
- Philippot P. and Selverstone J. (1991) Trace-element-rich brines in eclogitic veins: implications for fluid composition and transport during subduction. *Contrib. Mineral. Petr.* **106**(4), 417–430.
- Philippot P., Chevallier P., Chopin C. and Dubessy J. (1995) Fluid composition and evolution in coesite-bearing rocks (Dora-Maira massif, Western Alps): implications for element recycling during subduction. *Contrib. Mineral. Petr.* **121**(1), 29.
- Plank T. and Manning C. E. (2019) Subducting carbon. *Nature* **574** (7778), 343–352.
- Roedder E. (1984) *Volume 12: Fluid Inclusions*. Mineralogical Society of America, Chantilly (USA), pp. 646.
- Rubatto D. and Hermann J. (2001) Exhumation as fast as subduction? *Geology* **29**(1), 3–6.
- Sanchez-Valle C. (2013) Structure and thermodynamics of subduction zone fluids from spectroscopic studies. In *Thermodynamics of Geothermal Fluids* (eds. Stefánsson A.; Driesner T.; Bénédeth P.) *Reviews in Mineralogy and Geochemistry*, **76**(1), 265–309.
- Sterner S. M. and Pitzer K. S. (1994) An equation of state for carbon dioxide valid from zero to extreme pressures. *Contrib. Mineral. Petr.* **117**(4), 362–374.
- Stöckhert B., Duyster J., Trepmann C. and Massonne H. J. (2001) Microdiamond daughter crystals precipitated from supercritical COH+ silicate fluids included in garnet, Erzgebirge, Germany. *Geology* **29**(5), 391–394.
- Svensen H., Jamtveit B., Yardley B., Engvik A. K., Austrheim H. and Broman C. (1999) Lead and bromine enrichment in eclogite-facies fluids: extreme fractionation during lower-crustal hydration. *Geology* **27**(5), 467–470.
- Sverjensky D. A., Harrison B. and Azzolini D. (2014) Water in the deep Earth: the dielectric constant and the solubilities of quartz and corundum to 60 kb and 1200 C. *Geochim. Cosmochim. Acta* **129**, 125–145.
- Tarling M. S., Rooney J. S., Viti C., Smith S. A. and Gordon K. C. (2018) Distinguishing the Raman spectrum of polygonal serpentine. *J. Raman. Spectrosc.* **49**(12), 1978–1984.
- Touret J. L. R. (2001) Fluids in metamorphic rocks. *Lithos* **55**(1–4), 1–25.
- Tumiati S. and Malaspina N. (2019) Redox processes and the role of carbon-bearing volatiles from the slab–mantle interface to the mantle wedge. *J. Geol. Soc. London* **176**(2), 388–397.
- van Schroyen Lantman H. W., Scambelluri M., Gilio M., Wallis D. and Alvaro M. (2021) Extensive fluid–rock interaction and pressure solution in a UHP fluid pathway recorded by garnetite, Lago di Cignana, Western Alps. *J. Metamorph. Geol.* **39**(4), 501–518.
- Vitale Brovarone A. V., Martinez I., Elmaleh A., Compagnoni R., Chaduteau C., Ferraris C. and Esteve I. (2017) Massive production of abiotic methane during subduction evidenced in metamorphosed ophicarbonates from the Italian Alps. *Nat. Commun.* **8**(1), 1–13.
- Whitney D. L. and Evans B. W. (2010) Abbreviations for names of rock-forming minerals. *Am. Mineral.* **95**(1), 185–187.
- Zhang Z. M., Shen K., Sun W. D., Liu Y. S., Liou J. G., Shi C. and Wang J. L. (2008) Fluids in deeply subducted continental crust: petrology, mineral chemistry and fluid inclusion of UHP metamorphic veins from the Sulu orogen, eastern China. *Geochim. Cosmochim. Acta* **72**(13), 3200–3228.

Associate editor: Weidong Sun